nature portfolio

https://doi.org/10.1038/s41929-022-00797-0

Supplementary information

Experimental Sabatier plot for predictive design of active and stable Pt-alloy oxygen reduction reaction catalysts

In the format provided by the authors and unedited

Supplementary Information to

Experimental Sabatier plot for predictive design of active and stable Pt-alloy oxygen reduction reaction catalysts

Jin Huang[1], Luca Sementa[2], Zeyan Liu[1], Giovanni Barcaro[2], Miao Feng[1,3], Ershuai Liu[4], Li Jiao[4], Mingjie Xu[5,6], Denis Leshchev[7], Sung-Joon Lee[1], Mufan Li[8], Chengzhang Wan[8], Enbo Zhu[1], Yang Liu[1], Bosi Peng[8], Xiangfeng Duan[8,9], William A. Goddard III[10]*, Alessandro Fortunelli[2]*, Qingying Jia[4]*, Yu Huang[1,9]*

[1]Department of Materials Science and Engineering, University of California, Los Angeles; Los Angeles, CA 90095, USA.

[2]CNR-ICCOM & IPCF, Consiglio Nazionale delle Ricerche; Pisa, I-56124, Italy.

[3]College of Materials Science and Engineering, Fuzhou University, 2 Xueyuan Road, Fuzhou, Fujian, 350108, P. R. China.

[4]Department of Chemistry and Chemical Biology, Northeastern University; Boston, MA 02115, USA.

[5]Irvine Materials Research Institute, University of California, Irvine; Irvine, CA 92697, USA.

[6]Department of Materials Science, University of California, Irvine; Irvine, CA 92697, USA.

[7]National Synchrotron Light Source II, Brookhaven National Laboratory; Upton, New York 11973, USA.

[8]Department of Chemistry and Biochemistry, University of California, Los Angeles; Los Angeles, CA 90095, USA.

[9]California NanoSystems Institute, University of California, Los Angeles; Los Angeles, CA 90095, USA.

[10]Materials and Process Simulation Center, California Institute of Technology; Pasadena, CA 91125, USA.

*Corresponding author. Email: yhuang@seas.ucla.edu (Y.H.); qjia@iit.edu (Q.J.); alessandro.fortunelli@cnr.it (A.F.); wag@wag.caltech.edu (W.A.G.).

This PDF file includes:

Supplementary Notes 1

Building a binary experimental descriptor (BED) for strain and Pt-M coupling effects

Strain descriptor:

Since the tight-binding matrix element[1] of a Pt atom in an alloy scales as:

$$Vi = 7.62 \times \sum_{j=1}^{CN} \frac{\left(r_{d,i} r_{d,j}\right)^{1.5}}{(dpt_{ij}^{5})} \quad (1)$$

where the given atom "i" with radius $r_{d,i}$ is surrounded by "j" first-neighbors with radius $r_{d,j}$ each at a distance $d_{Pt,ij}$ and the sum over "j" runs over the coordination number (CN) of the given Pt atom. Taking a PtNi alloy as an example,

$$Vi(Pt) = 7.62\ (r_d^{Pt})^3 \{\sum_{j=1}^{NN_{Pt}} \frac{1}{\left(d_{ij}^{Pt-Pt}\right)^5} + \left(\frac{r_d^{Ni}}{r_d^{Pt}}\right)^{3/2} \sum_{j=1}^{NN_{Ni}} \frac{1}{\left(d_{ij}^{Pt-Ni}\right)^5}\} \quad (2)$$

where the sums in Eq. (2) run over the NN_{Pt} Pt nearest-neighbors or the NN_{Ni} Ni nearest-neighbors of the Pt atom "i".

We now introduce d_0^{Pt-Pt} and d_0^{Pt-Ni} as reference nearest-neighbor inter-atomic distances for Pt-Pt and Pt-Ni interactions, respectively, and transform the d_{ij} distances into the corresponding strain s_{ij} , defined as:

$$s_{ij} = \frac{d_{ij} - d_0}{d_0}$$

So doing, we get in Eq. (2) terms of the form: $(1 + s_{ij})^{-5}$. We can expand these terms in a Taylor series or as a continued fraction or a mixture of these. We report below an expansion truncated to the linear term, and in square bracket the corresponding error with respect to the exact value 1.10629161708 for x = - 0.02 (a compressive strain of 2%):

$$\frac{1}{(1+x)^5} \approx 1 - 5x\ [0.006] \quad (3)$$

This first-order approximation gives a small error [0.006] and is therefore used to reflect strain descriptor [the correct next best estimate reads: 1 – 5x/(1 + 3 x)]. We therefore use the first-order linear expansion, and we finally get:

$$V_i(Pt) = V_i^0(Pt) - 7.62 \cdot 5 \cdot \frac{\left(r_d^{Pt}\right)^3}{\left(d_0^{Pt-Pt}\right)^5} \cdot \{\sum_{j=1}^{NN_{Pt}} s_{ij}^{Pt-Pt} + \left(\frac{r_d^{Ni}}{r_d^{Pt}}\right)^{3/2} \frac{\left(d_0^{Pt-Pt}\right)^5}{\left(d_0^{Pt-Ni}\right)^5} \sum_{j=1}^{NN_{Ni}} s_{ij}^{Pt-Ni}\} \quad (4)$$

Note that the d-band center shift correlates with the matrix element difference [1] compared to pure unstrained Pt:

$$\Delta\varepsilon_d = |\varepsilon_d(PtM) - \varepsilon_d(Pt)| \propto \Delta Vi \quad (5)$$

For our experimentally measured strain, we used the Pt-Pt bond length measured in XAS to calculate the strain and kept the same definition as in the simulation:

$$Strain = \frac{R_{Pt-Pt}(PtM) - R_{Pt-Pt}(Pt/C)}{R_{Pt-Pt}(Pt/C)} \times 100\% \quad (6)$$

$R_{Pt\text{-}Pt}$ (Pt/C) is 2.75 Å according to XAS measurement. The compressive strain is defined as the absolute value of strain if strain is below 0.

The issue with formula (4) and (5) is that it is difficult to accurately obtain the Pt-Ni strain experimentally due to the composition difference of catalysts (the reference d_{ij}^{Pt-Ni} is not a constant and changes with composition). Therefore, the pre-factor for the term of the matrix element proportional to the Pt-Ni strain part *varies for each catalyst*. In addition, it is even more challenging to describe the matrix elements of multi-elemental Pt alloys since *strain terms of different origin are involved*. Therefore, a descriptor that can reflect the contribution from other metals would be highly desirable. In this study, we propose that the asymmetry factor (AF) of the XANES peak is a good candidate, which comprehensively reflects the Pt-M coupling that includes the contributions from composition and local atomic contribution of Pt-M bonding from the M side.

We then introduce another descriptor to describe the contribution from the alloying metals, the AF.

Supplementary Notes 2

Asymmetry factor (AF) descriptor:

The asymmetry factor (AF) of the XANES peaks is calculated with the equation: AF = b/a,

where:

b is the distance from the peak midpoint (perpendicularly from the peak highest point) to the trailing edge of the peak measured at 10% of peak height，

a is the distance from the leading edge of the peak to the peak midpoint.

The trailing edge is determined by taking the first derivative of the Pt L_3 XANES. For example, in Supplementary Fig. 1, trailing edge of the peak is chosen around 11576 eV for Pt/C and around 11577 eV for Pt-alloy catalysts, respectively. Corresponding intensity was then set as the peak bottom. The difference of the peak intensity and the above determined bottom intensity is the peak height.

In the alloy case, we calculate the difference in AF with respect to pure Pt, i.e., Δ(asymmetry factor) of PtM: $\Delta AF = AF(PtM) - AF(Pt/C)$

All the calculated ΔAF can be found in Supplementary Table 3.

Supplementary Notes 3

The binary experimental descriptor (BED):

To quantitatively determine the relationship between ΔE_O and the binary experimental descriptor (BED) (i.e., to determine the relative weights in the combination of Strain (%) and ΔAF), we performed the linear fitting:

$$BED = A\big(Strain\ (\%)\big) + B(\Delta AF) \tag{7}$$

By fitting [$\Delta E_O^{(111)}$ - $\Delta E_O^{Pt(111)}$] with the BED enforcing the intercept (0, 0) and a one-to-one correspondence relationship, the optimal A and B are determined to be -0.13 and 0.1, respectively with a high fidelity (R^2 = 0.93) and a low root-mean-square error (RMSE) of 0.03 eV (Fig. 2C), thus achieving a better fit than when using only the strain as a descriptor (fidelity of 0.82 and RMSE of 0.04 eV) (Supplementary Fig. 14).

So, our final binary descriptor is determined to be:

$$BED = [-0.13\big(Strain\ (\%)\big) + 0.1(\Delta AF)] \tag{8}$$

Supplementary Figures

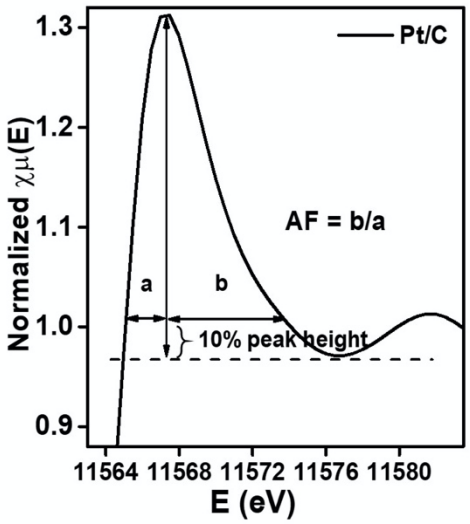

Supplementary Fig. 1 | A typical asymmetry factor calculation from XANES of Pt/C catalysts.

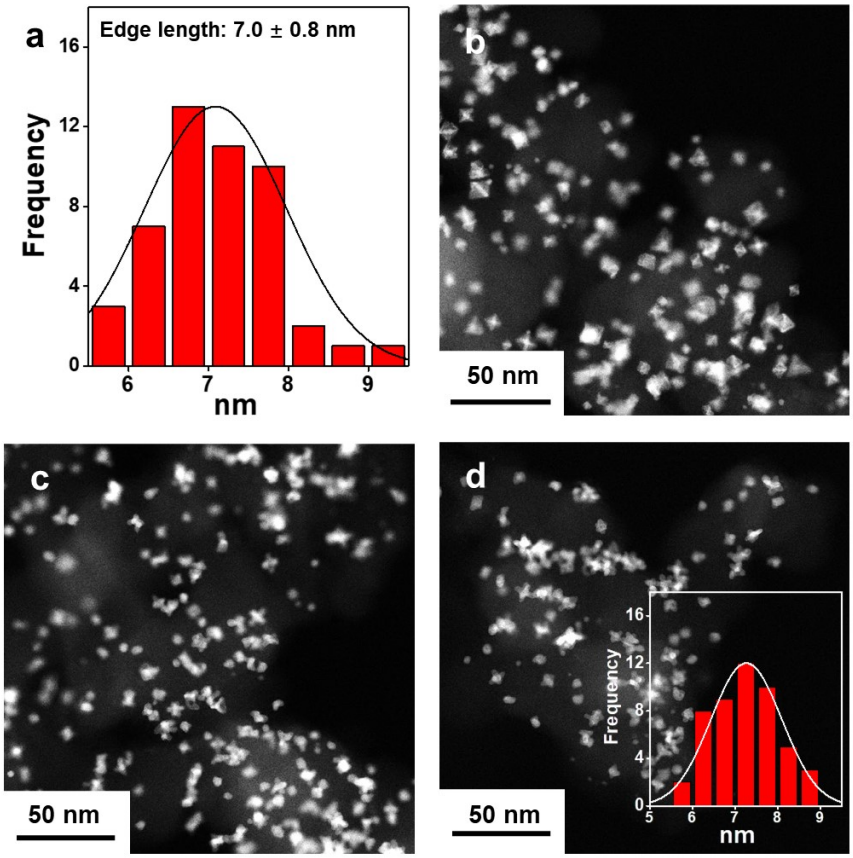

Supplementary Fig. 2 | TEM analysis of sd-PtNi catalysts at different stages. (**a**) Size distribution of octahedral p-$Pt_{45}Ni_{55}$ catalysts. (**b-d)** Representative HAADF-STEM images for p-$Pt_{45}Ni_{55}$, sd-$Pt_{76}Ni_{24}$, and sd-$Pt_{85}Ni_{15}$, respectively. The inset of the panel (**d**) is the size distribution of sd-$Pt_{85}Ni_{15}$, diagonal distance is the longest distance between two diagonal branched tips.

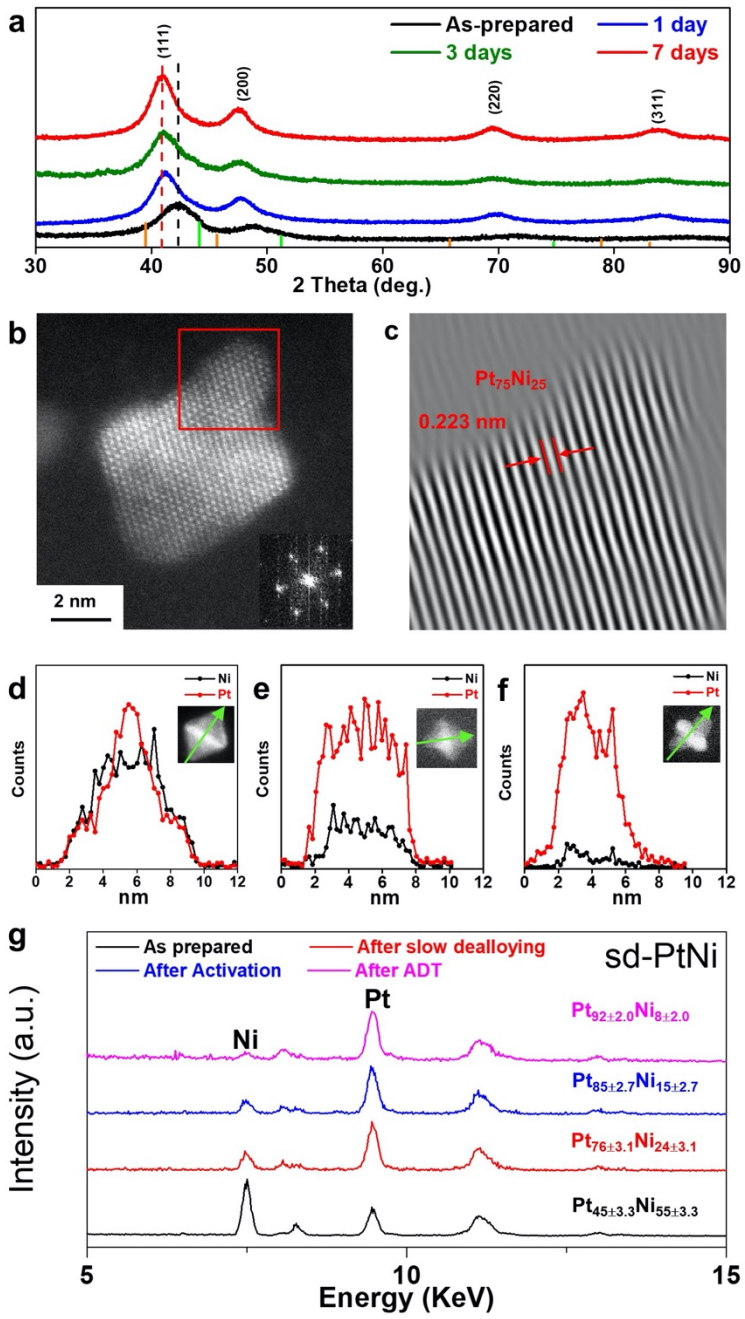

Supplementary Fig. 3 | Structural and compositional characterization of sd-PtNi catalysts during the slow dealloying process. (**a**) XRD patterns of sd-PtNi catalysts at different dealloying time. Orange line and green line represent Pt [PDF #04-0802] and Ni [PDF #04-0850], respectively. (**b**) High-resolution atomic HAADF-STEM images of sd-$Pt_{76}Ni_{24}$ catalysts. (**c**) Corresponding inverse FFT images of sd-$Pt_{76}Ni_{24}$ catalysts (the red square region in the panel (**c**)). (**d-f**) Representative EDX line-scan profile for p-$Pt_{45}Ni_{55}$, sd-$Pt_{76}Ni_{24}$, and sd-$Pt_{85}Ni_{15}$, respectively. The insets of the (**d-f**) are the corresponding HAADF-STEM images. (**g**) EDX compositional analysis of sd-PtNi catalysts at different stages. Each stage corresponds to p-$Pt_{45}Ni_{55}$ (black), sd-$Pt_{76}Ni_{24}$ (red), sd-$Pt_{85}Ni_{15}$ (blue), and sd-$Pt_{92}Ni_{8}$-ADT (pink), respectively.

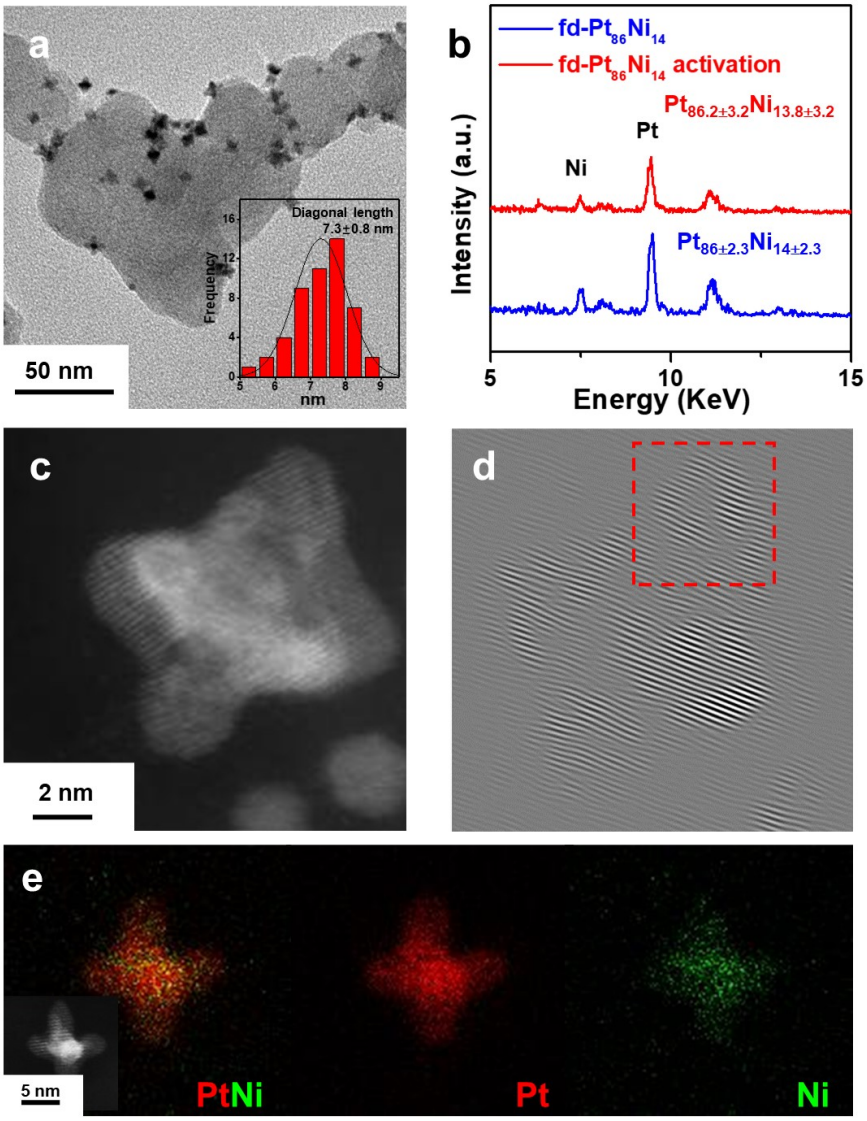

Supplementary Fig. 4 | Structural and compositional analysis of the fd-$Pt_{86}Ni_{14}$ catalysts. (**a**) TEM of the fd-$Pt_{86}Ni_{14}$ catalysts before activation. (**b**) EDX composition analysis of the fd-$Pt_{86}Ni_{14}$ catalysts before and after activation, showing no obvious difference due to sufficient acid dealloying. (**c**) HAADF-STEM image of the fd-$Pt_{86}Ni_{14}$ catalysts. (**d**) Inverse fast Fourier transform (FFT) of the corresponding fd-$Pt_{86}Ni_{14}$ catalysts in the panel (**c**), showing similar Pt skin structure after fast acid dealloying. (**e**) EDX mapping results of the fd-$Pt_{86}Ni_{14}$ catalysts before activation.

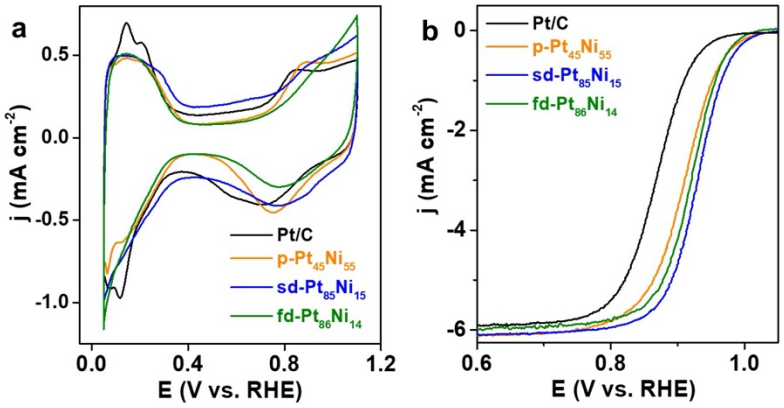

Supplementary Fig. 5 | Electrochemical measurement of p-$Pt_{45}Ni_{55}$, sd-$Pt_{85}Ni_{15}$, and fd-$Pt_{86}Ni_{14}$ versus commercial Pt/C catalysts. (**a**) CVs of p-$Pt_{45}Ni_{55}$ (orange), sd-$Pt_{85}Ni_{15}$ (blue), and fd-$Pt_{86}Ni_{14}$ (olive) versus commercial Pt/C catalysts (black) recorded at room temperature in N_2-purged 0.1 M $HClO_4$ solution at a sweep rate of 100 mV/s from 0.05 to 1.1 V vs. RHE. (**b**) ORR polarization curves of p-$Pt_{45}Ni_{55}$ (orange), sd-$Pt_{85}Ni_{15}$ (blue), and fd-$Pt_{86}Ni_{14}$ catalysts (olive) in comparison to Pt/C catalysts (black). The ORR tests were measured in O_2-purged 0.1 M $HClO_4$ solution at a sweep rate of 20 mV/s from 0.05 to 1.1 V vs. RHE.

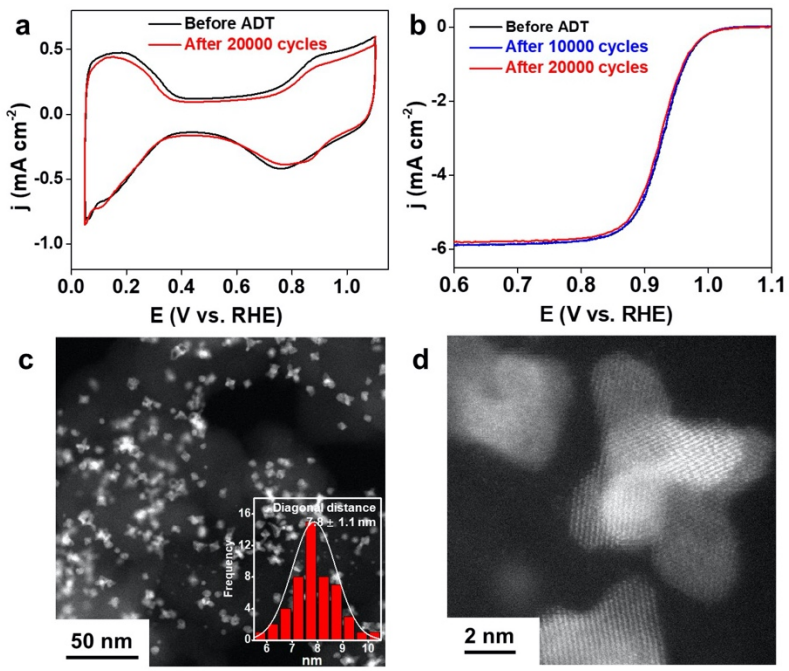

Supplementary Fig. 6 | Electrochemical stability analysis of sd-$Pt_{85}Ni_{15}$ catalysts. (**a**) CV curves of sd-$Pt_{85}Ni_{15}$ catalysts before (black) and after 20,000 cycles ADT (red). (**b**) ORR polarization curves of sd-$Pt_{85}Ni_{15}$ catalysts before stability test (black), after 10,000 cycles ADT (blue), and after 20,000 cycles ADT (red). (**c, d**) Representative HAADF-STEM and high-resolution HAADF-STEM image of the sd-PtNi after 20,000 cycles ADT, the inset of the panel (**c**) is the size distribution of sd-PtNi after ADT, diagonal distance is the longest distance of two diagonal branched tips. The diagonal distance slightly increased from 7.2 nm to 7.8 nm without obvious growth for each branch, suggesting good structural and morphology stability.

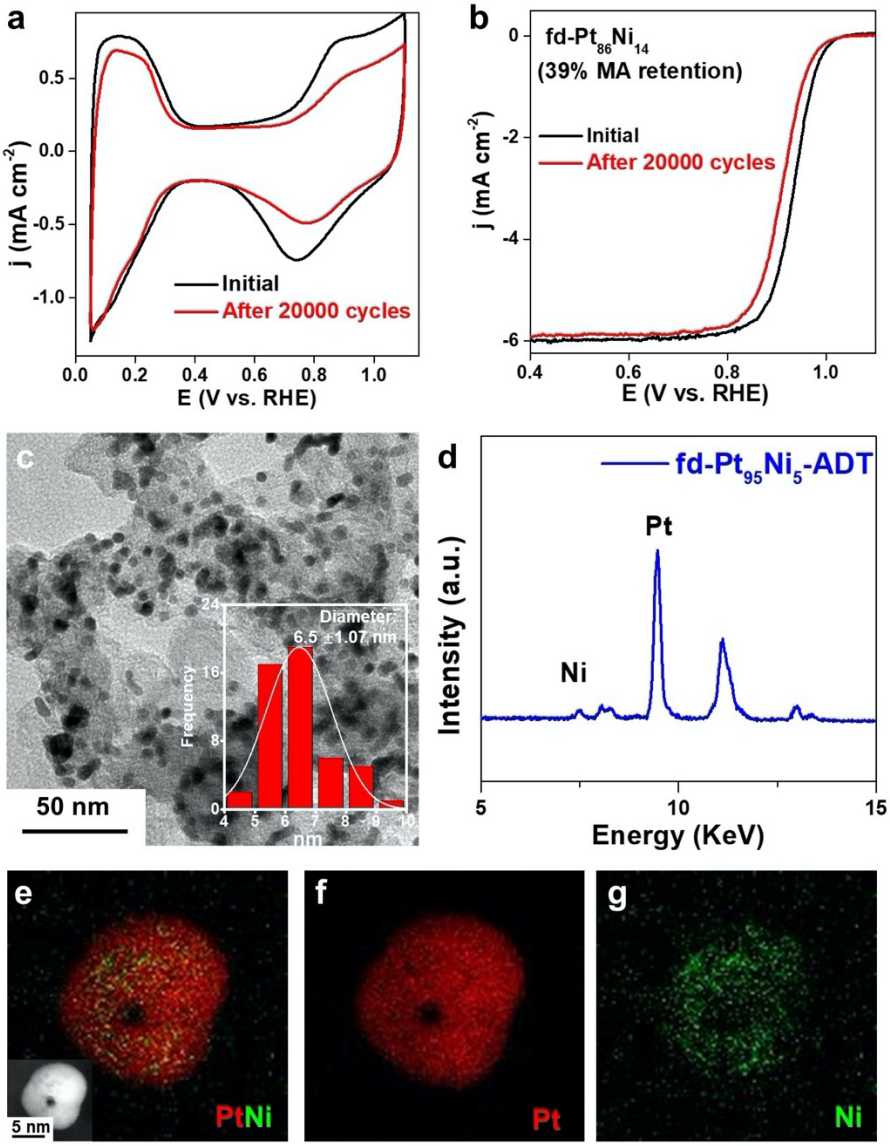

Supplementary Fig. 7 | Electrochemical stability analysis of fd-$Pt_{86}Ni_{14}$. (**a**) CV curves of fd-$Pt_{86}Ni_{14}$ catalysts before (black) and after 20,000 cycles ADT (red). (**b**) ORR polarization curves of fd-$Pt_{86}Ni_{14}$ catalysts before (black) and after 20,000 cycles ADT (red). (**c**) TEM image of fd-$Pt_{86}Ni_{14}$ after 20,000 cycles ADT, the inset of panel (**c**) is the size distribution of fd-$Pt_{95}Ni_5$-ADT. (**d**) EDX spectrum of the fd-$Pt_{86}Ni_{14}$ after 20,000 cycles ADT. (**e-g**) EDX mapping results of fd-$Pt_{95}Ni_5$-ADT after 20,000 cycles ADT, the inset of panel (**e**) is the HRTEM.

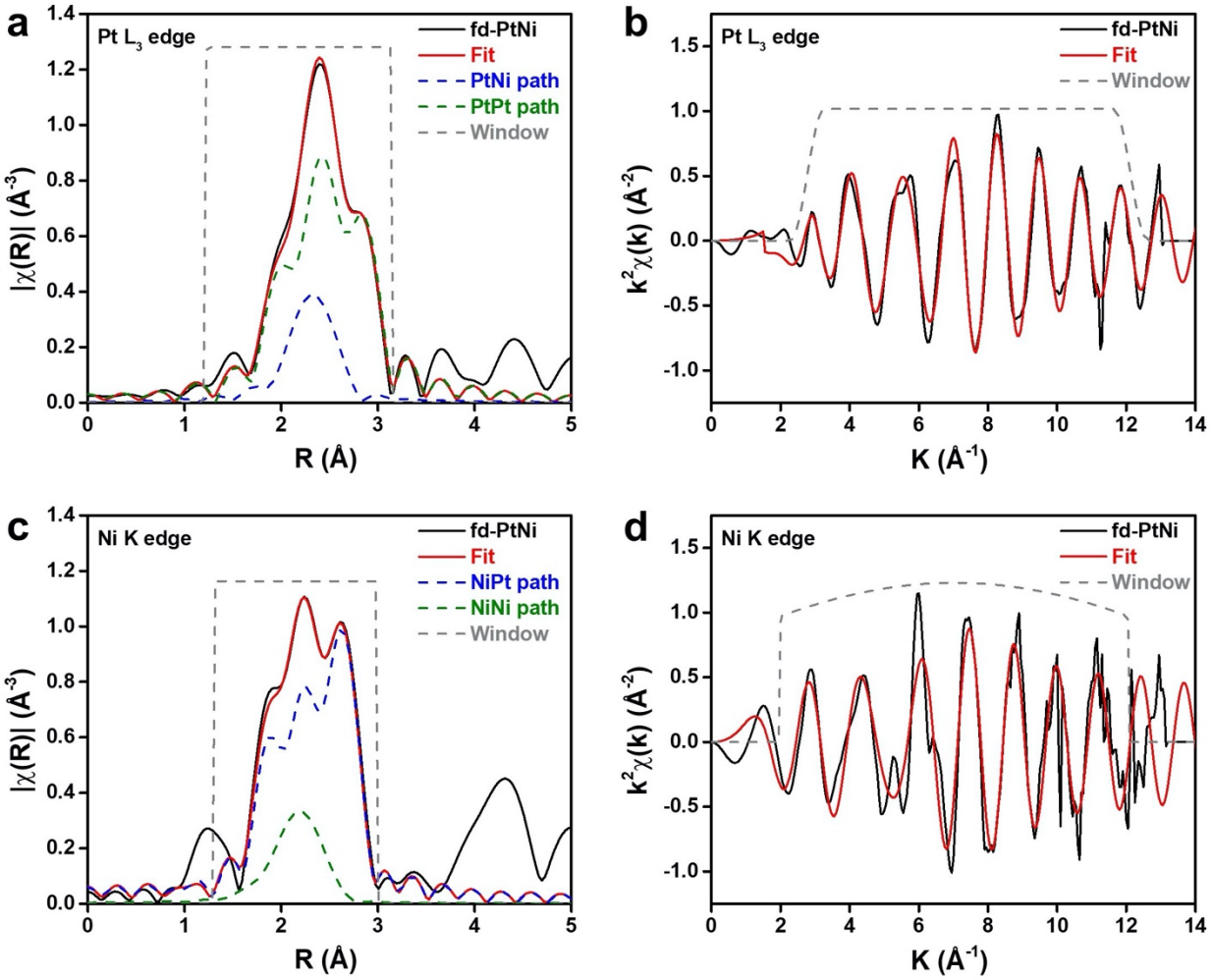

Supplementary Fig. 8 | In situ FT-EXAFS spectra at the Pt L_3-edge at the (a) R-space and (b) K-space and Ni K-edge at the (c) R-space and (d) K-space of fd-PtNi collected at 0.54 V in O_2-purged 0.1 M $HClO_4$ and their fits. Fits were performed at the Pt L_3 and Ni K-edge simultaneously in *R*-space, $k^{1,2,3}$ weighting. $1.2 < R < 3.1$ Å and $\Delta k = 2.8 – 12.2$ Å^{-1} for Pt spectra and $1.3 < R < 3.0$ Å and $\Delta k = 2.6 – 11.6$ Å^{-1} for Ni spectra were used for fitting. S_0^2 was fixed at 0.84 and 0.68 for Pt and Ni, respectively, as obtained by fitting the corresponding reference foils.

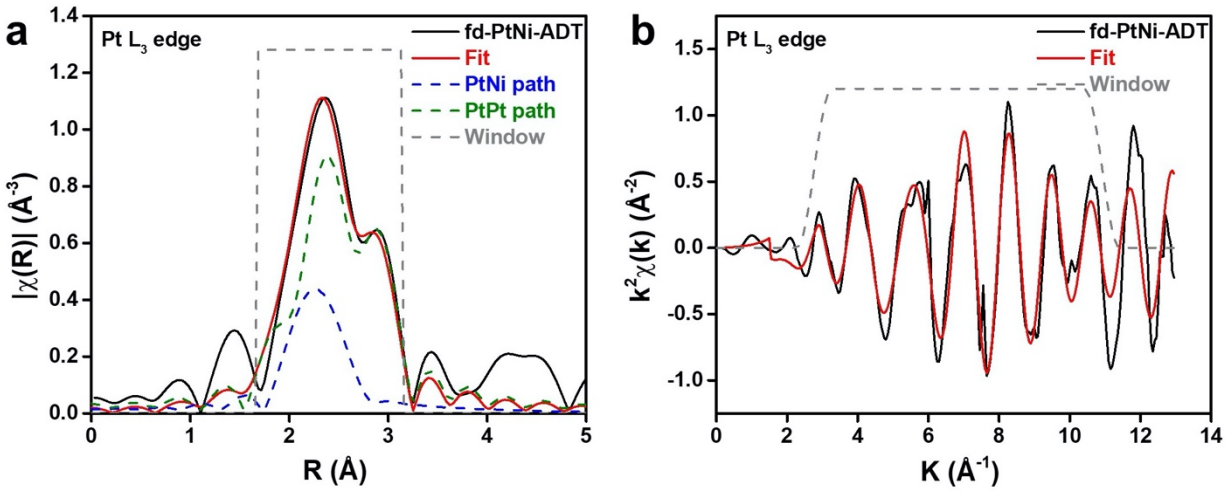

Supplementary Fig. 9 | In situ FT-EXAFS spectra at the Pt L_3-edge at the (a) R-space and (b) K-space of fd-PtNi-ADT collected at 0.54 V in O_2-purged 0.1 M $HClO_4$ and their fits. Fits were performed at the Pt L_3 in *R*-space, $k^{1,2,3}$ weighting. $1.68 < R < 3.14$ Å and $\Delta k = 2.77 – 10.92$ Å^{-1} were used for fitting. S_0^2 was fixed at 0.84 for Pt, as obtained by fitting the corresponding reference foil. Note here we did not fit the Ni K-edge data owing to the mixed metal and oxide phases.

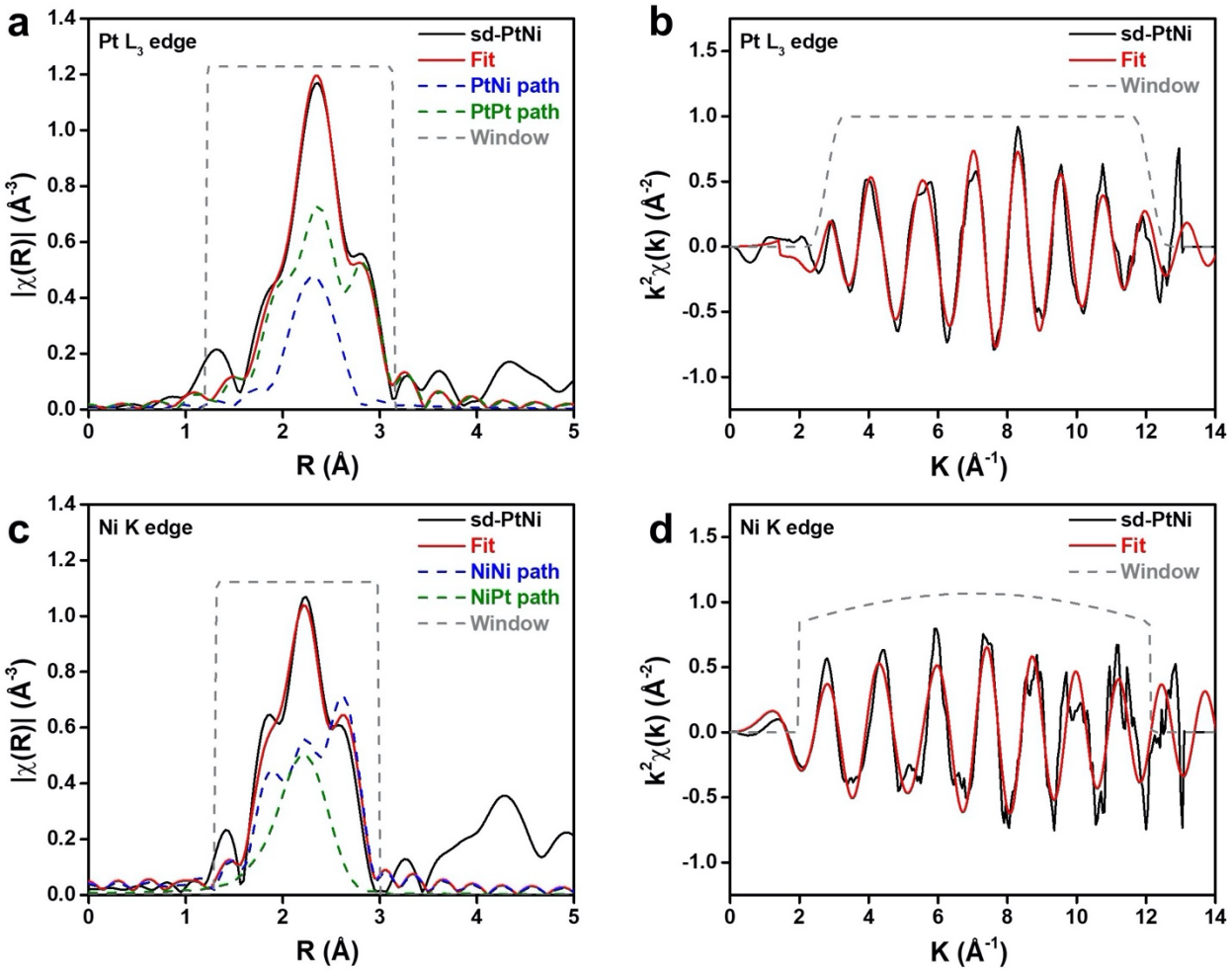

Supplementary Fig. 10 | In situ FT-EXAFS spectra at the Pt L_3-edge at the (a) R-space and (b) K-space and Ni K-edge at the (c) R-space and (d) K-space of sd-PtNi collected at 0.54 V in O_2-purged 0.1 M $HClO_4$ and their fits. Fits were performed at the Pt L_3 and Ni K-edge simultaneously in *R*-space, $k^{1,2,3}$ weighting. $1.2 < R < 3.1$ Å and $\Delta k = 2.8 – 12.2$ Å^{-1} for Pt spectra and $1.3 < R < 3.0$ Å and $\Delta k = 2.5 – 11.6$ Å^{-1} for Ni spectra were used for fitting. S_0^2 was fixed at 0.84 and 0.68 for Pt and Ni, respectively, as obtained by fitting the corresponding reference foils.

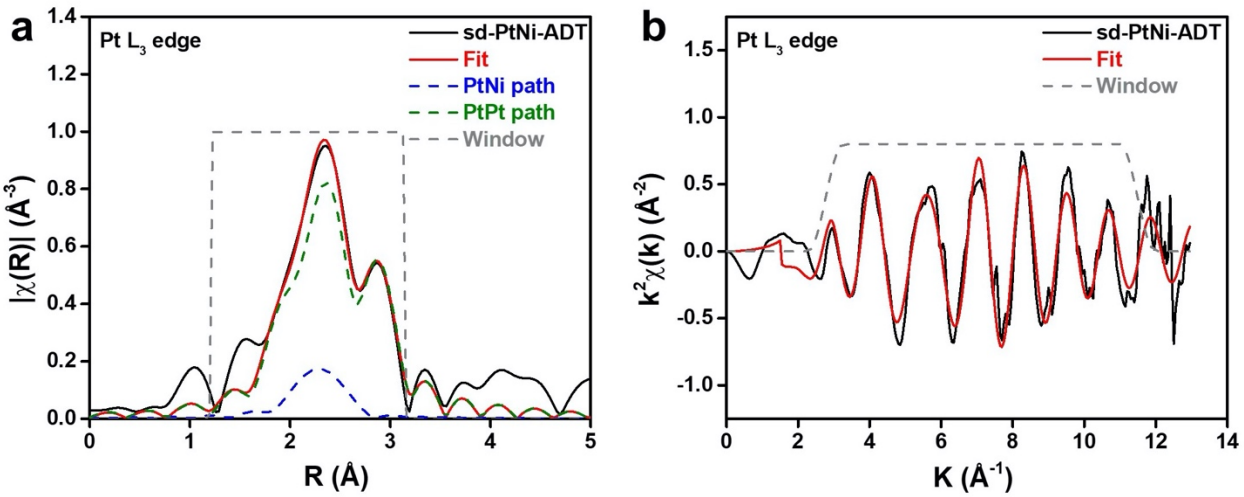

Supplementary Fig. 11 | In situ FT-EXAFS spectra at the Pt L_3-edge at the (a) R-space and (b) K-space of sd-PtNi-ADT collected at 0.54 V in O_2-purged 0.1 M $HClO_4$ and their fits. Fits were performed at the Pt L_3 in *R*-space, $k^{1,2,3}$ weighting. $1.22 < R < 3.14$ Å and $\Delta k = 2.77 - 11.49$ Å^{-1} were used for fitting. S_0^2 was fixed at 0.84 for Pt, as obtained by fitting the corresponding reference foil.

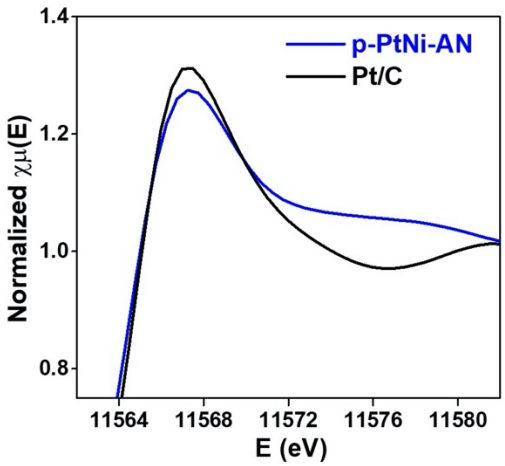

Supplementary Fig. 12 | XANES spectra of p-PtNi-AN (blue) and Pt/C catalysts (black). The p-PtNi-AN catalyst was activated in N_2-saturated 0.1 M $HClO_4$ between 0.05 V to 1.1 V versus RHE at a scan rate of 100 mV/s prior to XAS measurement.

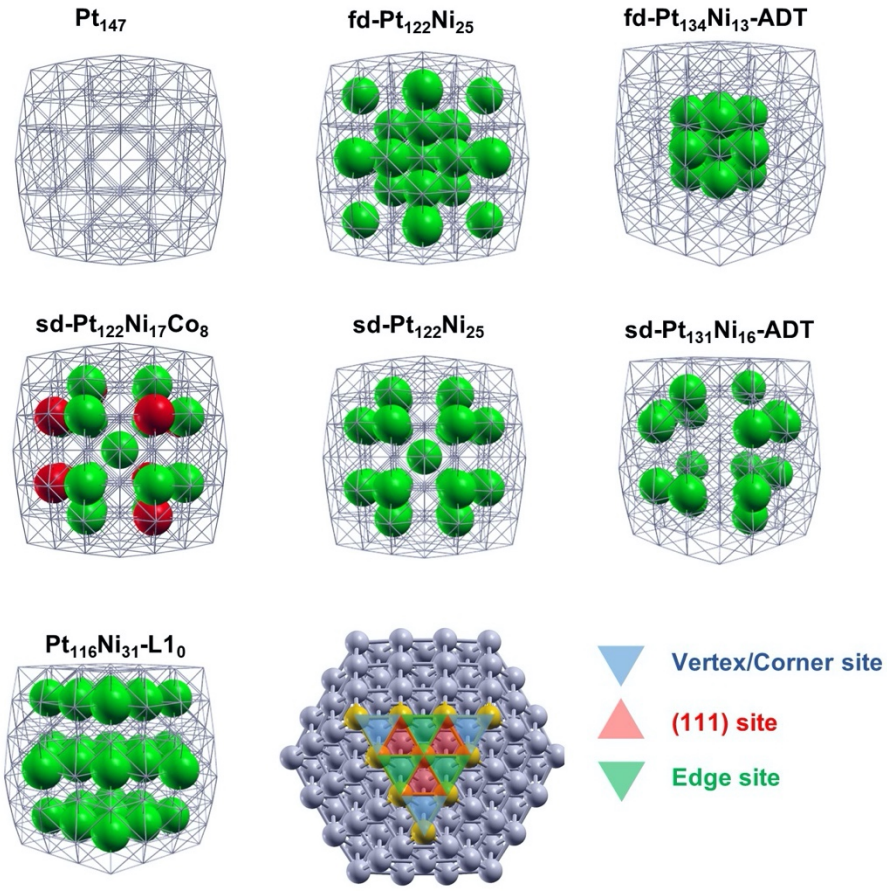

Supplementary Fig. 13 | Schematic depiction of the 147-atom cluster models investigated in this work together with the location of O-adsorption sites: (111) sites, edge sites, and vertex sites. The grey frame represents the Pt frame. Grey, green, and red sphere represent Pt, Ni and Co, respectively.

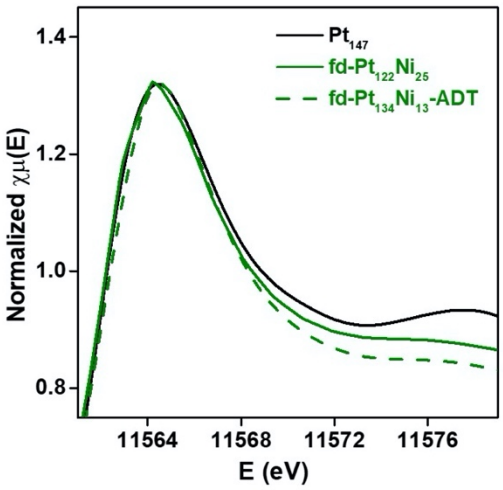

Supplementary Fig. 14 | FEFF9-derived Pt L_3-edge XANES spectra for Pt_{147} (black), fd-$Pt_{122}Ni_{25}$ (olive), and fd-$Pt_{134}Ni_{13}$-ADT (olive-dashed) cluster models. The XANES of fd-$Pt_{122}Ni_{25}$ and fd-$Pt_{134}Ni_{13}$-ADT were normalized to the height of the Pt_{147} model for comparison, showing no peak broadening.

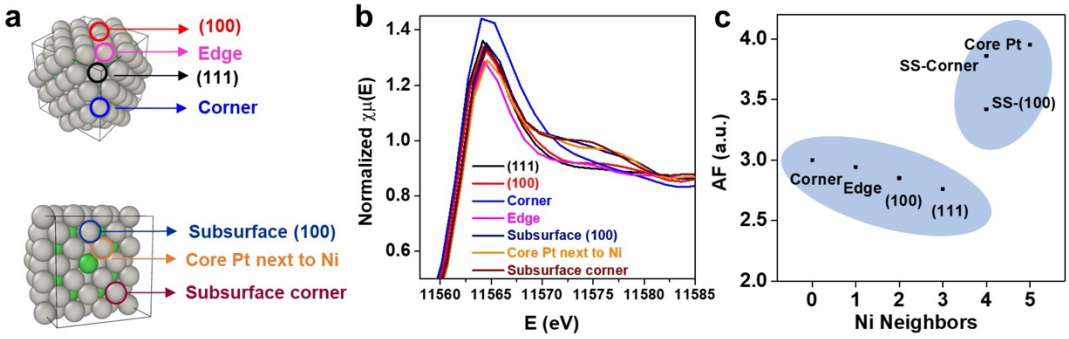

Supplementary Fig. 15 | (**a**) Depiction of specific sites of the mixed sd-$Pt_{122}Ni_{25}$ cluster. (**b**) Simulated XANES spectra by FEFF9 for the different sites of the sd-$Pt_{122}Ni_{25}$ model shown in (**a**). (**c**) The relationship between calculated AF and the number of Ni first-neighbors for different sites of the sd-$Pt_{122}Ni_{25}$ cluster model shown in (**a**), suggesting that Pt with more Ni neighbors generally showed a larger AF. SS-Corner: subsurface corner, SS-(111): subsurface (100), Core-Pt: Pt atoms located beneath the subsurface layer (the third layer).

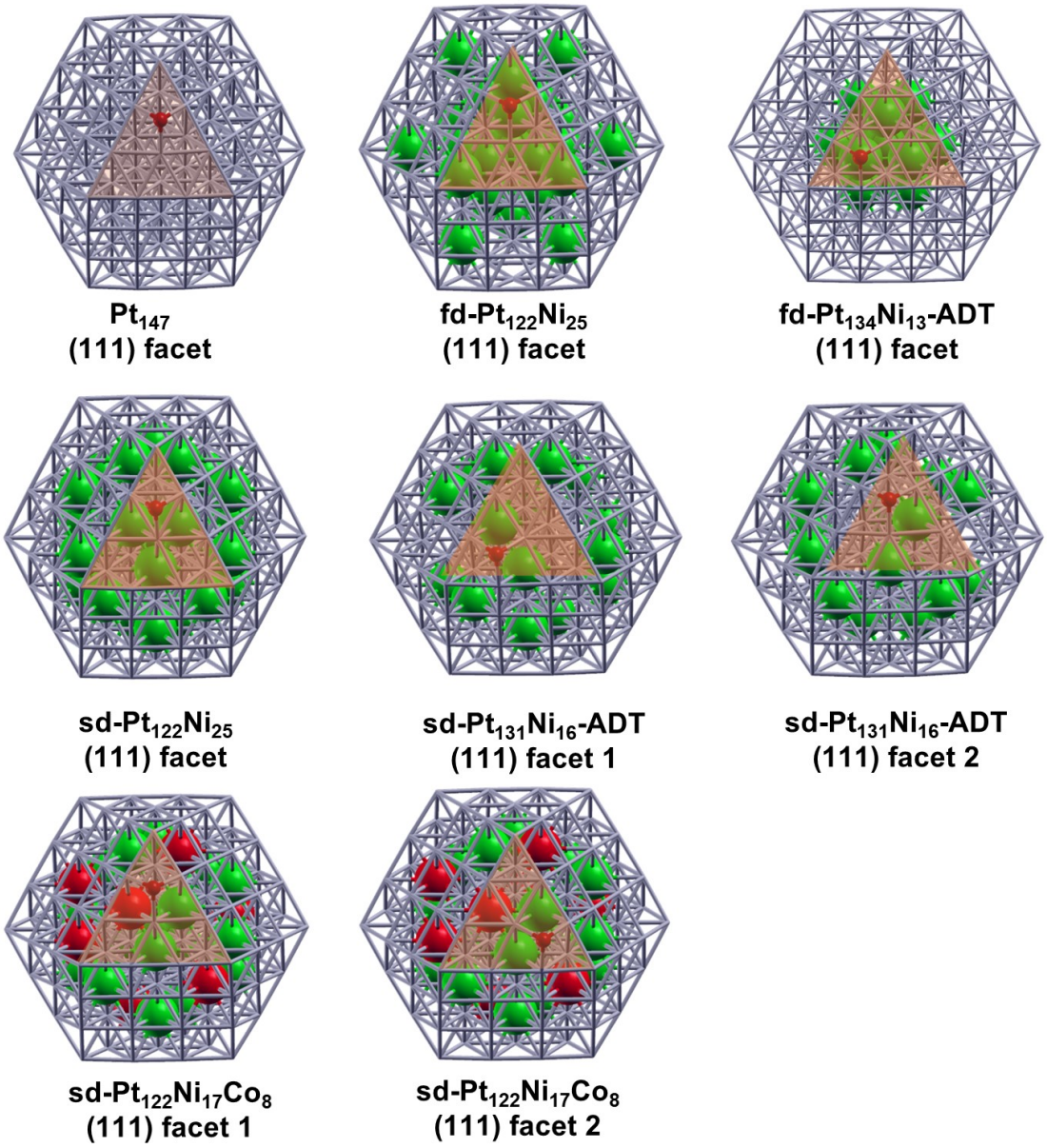

Supplementary Fig. 16 | Schematic depiction of 147-atom cluster models and O-binding on (111) sites. Note that in some cases there are 2 inequivalent adsorption sites, named as "facet 1" and "facet 2". In such cases, the oxygen binding energies reported in the main text are calculated as the average of oxygen binding energy of different (111) sites.

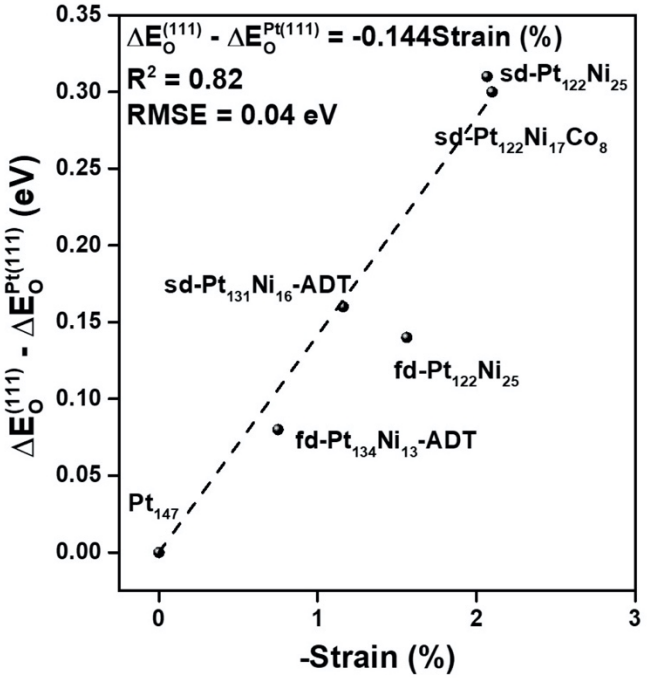

Supplementary Fig. 17 | Correlation between ($\Delta E_O^{(111)} - \Delta E_O^{Pt(111)}$) and (-Strain %), showing a R^2 of only 0.82. RMSE: Root-mean-square error.

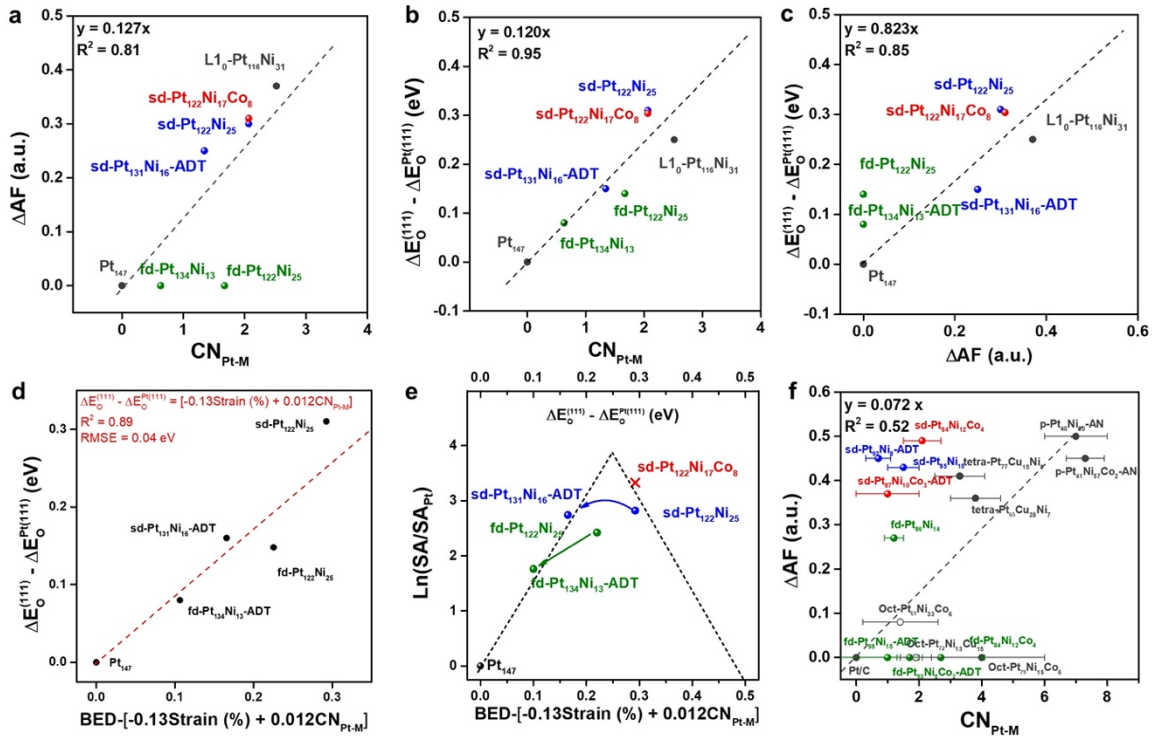

Supplementary Fig. 18 | CN analysis-based XANES data. (**a**) The correlation between $CN_{Pt\text{-}M}$ and ΔAF for cluster models, showing a good positive linear relationship. (**b**) The correlation between $CN_{Pt\text{-}M}$ and ($\Delta E_O - \Delta E_O^{Pt(111)}$) for theoretical models, showing a good linear one-to-one relationship. (**c**) The correlation between ΔAF and ($\Delta E_O - \Delta E_O^{Pt(111)}$) for theoretical models, showing a good linear one-to-one relationship. (**d**) Linear regression fitting between the DFT-determined ($\Delta E_O - \Delta E_O^{Pt(111)}$) and the BED-[-0.13Strain (%) + $0.012CN_{Pt\text{-}M}$] based on the cluster models, showing good one-to-one correspondence. RMSE: Root-mean-square error. (**e**) The Sabatier-like relationship between experimentally measured activity ($Ln(SA/SA_{Pt})$) with BED. (**f**) The plot of experimental $CN_{Pt\text{-}M}$ and experimental ΔAF, which shows no obvious correlation. The error bars were determined from the CN fitting of EXAFS.

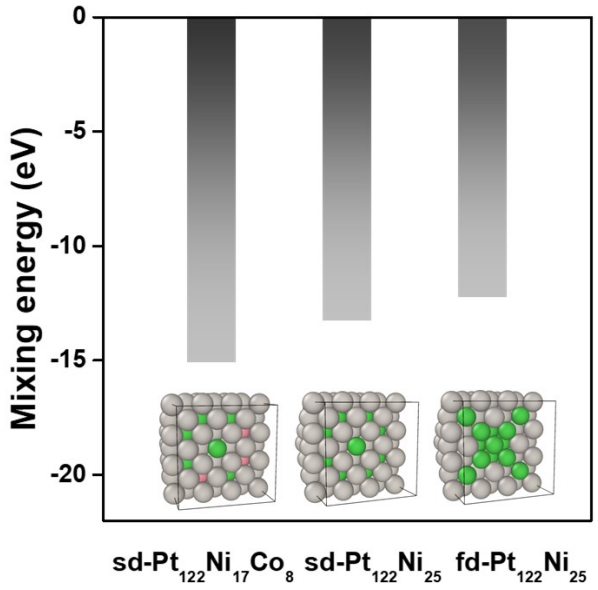

Supplementary Fig. 19 | Mixing energy of sd-$Pt_{122}Ni_{17}Co_8$ (left), sd-$Pt_{122}Ni_{25}$ (middle), and fd-$Pt_{122}Ni_{25}$ (right) clusters.

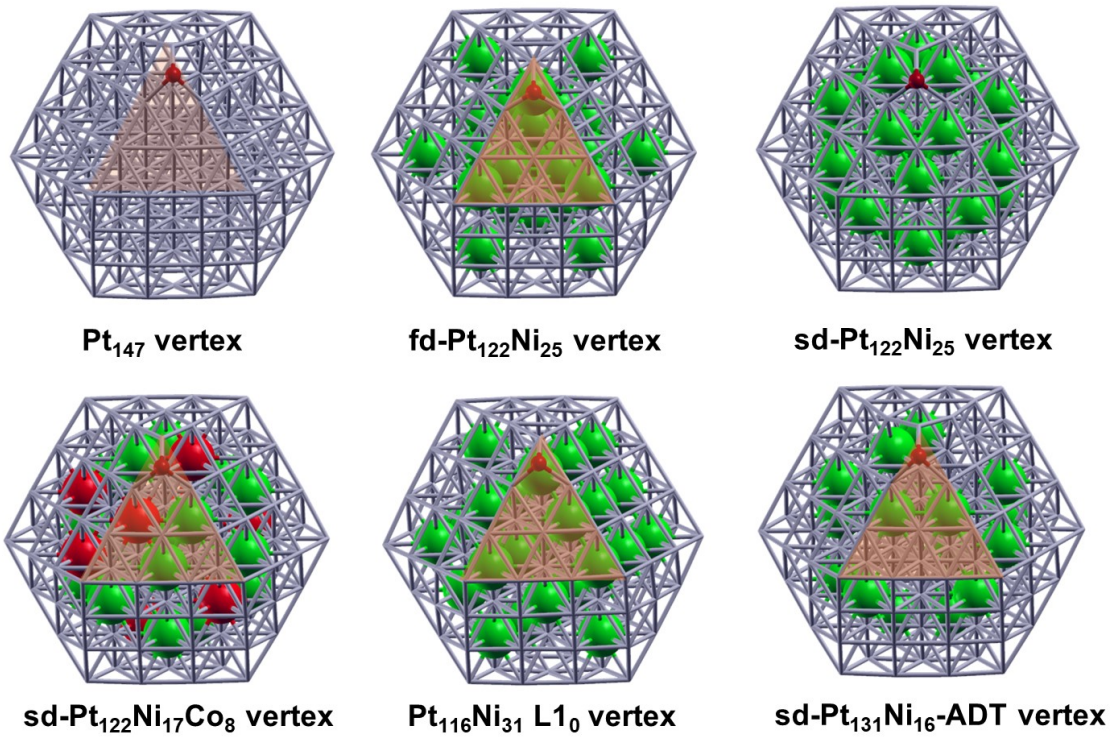

Supplementary Fig. 20 | Schematic depiction of 147-atom cluster models and O-binding on their vertex sites.

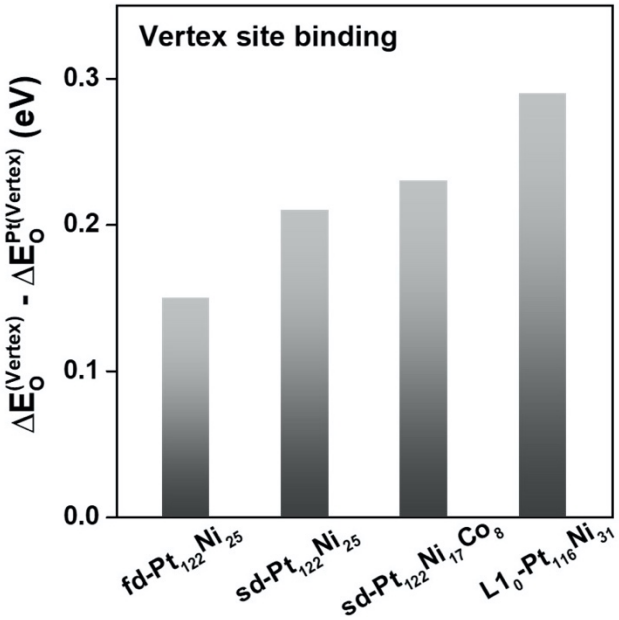

Supplementary Fig. 21 | Vertex site O-binding energy calculation results. The difference between $\Delta E_O^{(Vertex)}$ of Pt-alloy clusters and $\Delta E_O^{Pt(Vertex)}$ of the pure Pt cluster on vertex site for fd-$Pt_{122}Ni_{25}$, sd-$Pt_{122}Ni_{25}$, sd-$Pt_{122}Ni_{17}Co_8$, and $L1_0$-$Pt_{116}Ni_{31}$ 147-atom cluster models.

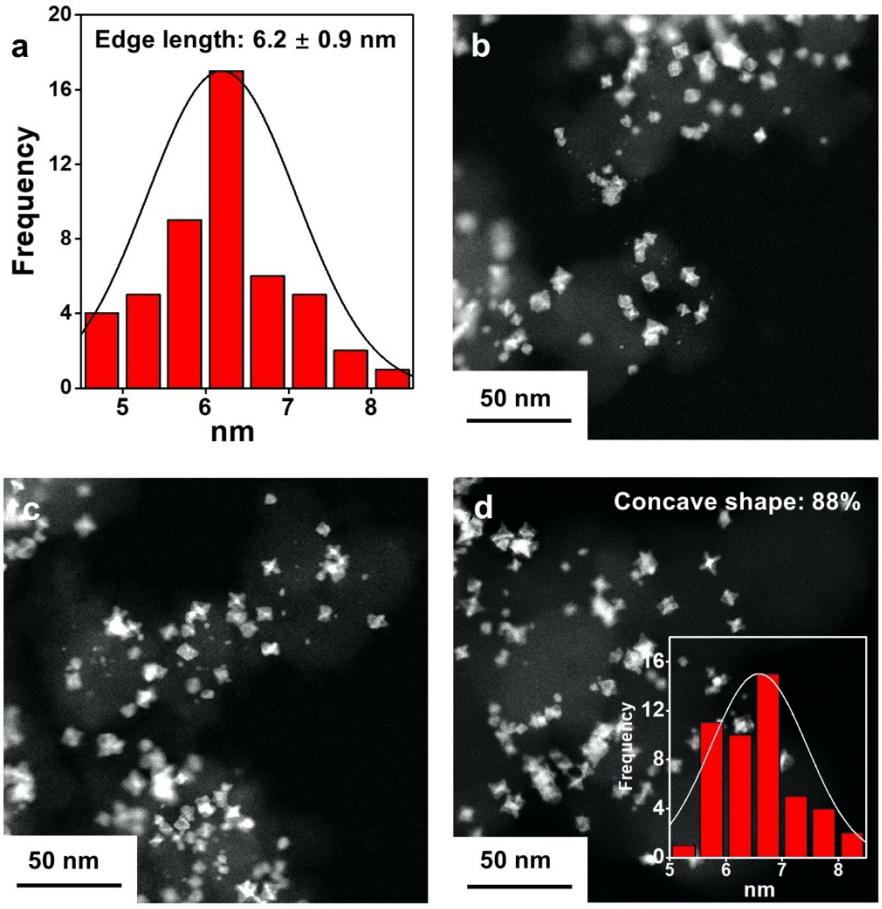

Supplementary Fig. 22 | TEM analysis of sd-PtNiCo catalysts at different stages. (**a**) Octahedra size distribution of p-$Pt_{41}Ni_{54}Co_5$ catalysts. (**b**-**d**) Representative HAADF-STEM images for p-$Pt_{41}Ni_{54}Co_5$, sd-$Pt_{70}Ni_{26}Co_4$, and sd-$Pt_{84}Ni_{12}Co_4$ after activation, inset of panel (**d**) is the size distribution of sd-$Pt_{84}Ni_{12}Co_4$ after activation. The insets of panel (**d**) are the percentage of concave shape and the size distribution, respectively.

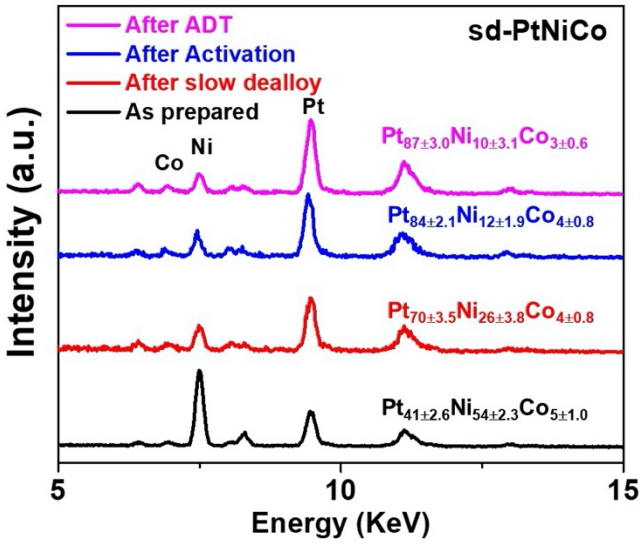

Supplementary Fig. 23 | EDX composition analysis of sd-PtNiCo at different stages. Each stage corresponds to p-$Pt_{41}Ni_{54}Co_5$ (black), sd-$Pt_{70}Ni_{26}Co_4$ (red), and sd-$Pt_{84}Ni_{12}Co_4$ (blue), and sd-$Pt_{87}Ni_{10}Co_3$-ADT (pink), respectively.

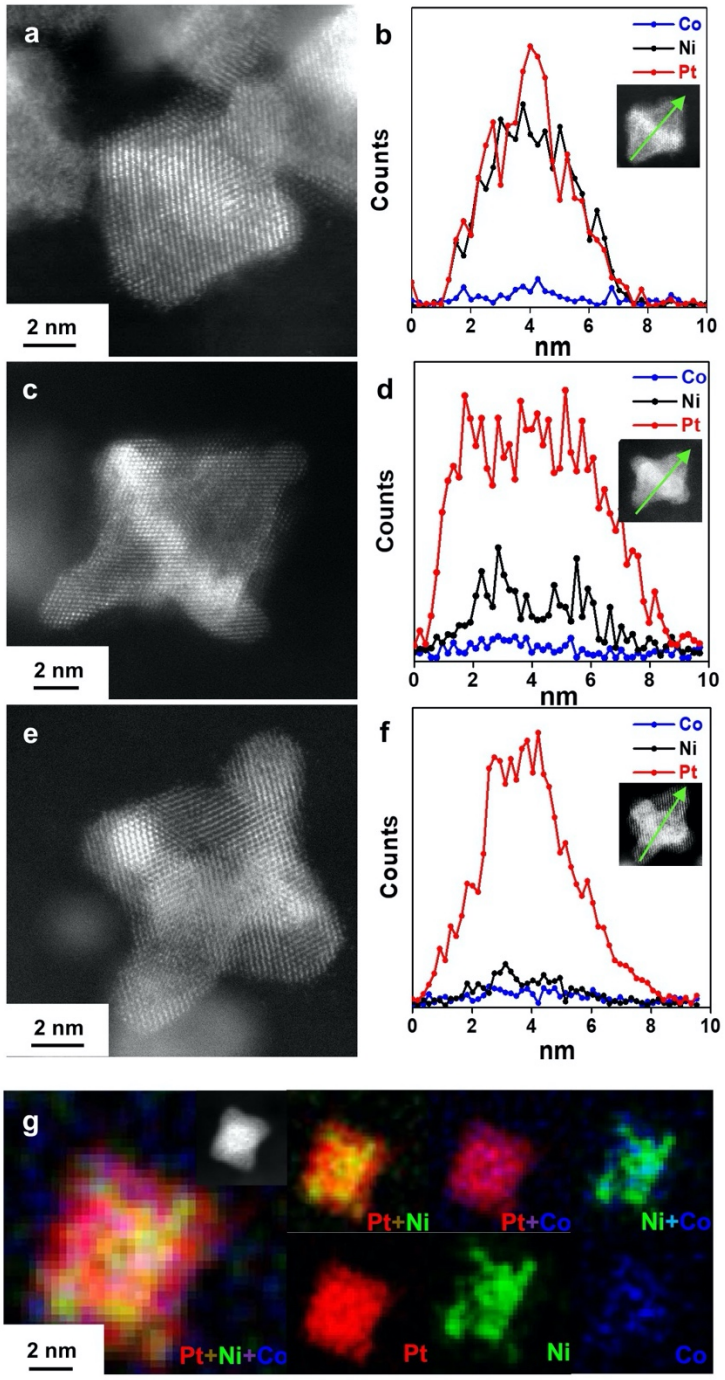

Supplementary Fig. 24 | Representative HAADF-STEM images and EDX line-scan and mapping analysis for (**a**, **b**) p-$Pt_{41}Ni_{54}Co_5$ catalyst, (**c**, **d**) sd-$Pt_{70}Ni_{26}Co_4$ catalyst (after slow-dealloying in DMF), and (**e, f**) sd-$Pt_{84}Ni_{12}Co_4$ catalysts (after activation). The insets in (**b, d, f**) are the corresponding HAADF-STEM images. (**g**) EDX mapping results of sd-$Pt_{84}Ni_{12}Co_4$ catalyst.

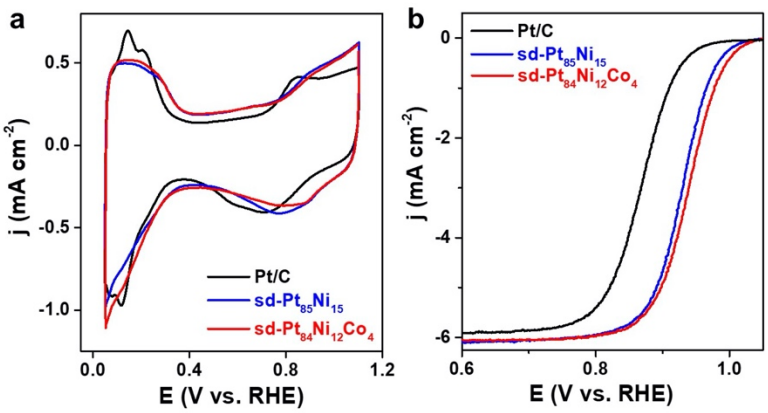

Supplementary Fig. 25 | Electrochemical performance of sd-$Pt_{84}Ni_{12}Co_4$ catalysts in comparison with sd-$Pt_{85}Ni_{15}$ and commercial Pt/C catalysts. (**a**) CVs of sd-$Pt_{85}Ni_{15}$ (blue) and sd-$Pt_{84}Ni_{12}Co_4$ (red) versus commercial Pt/C (black) catalysts recorded at room temperature in N_2-purged 0.1 M $HClO_4$ solution at a sweep rate of 100 mV/s. (**b**) ORR polarization curves of sd-$Pt_{85}Ni_{15}$ (blue) and sd-$Pt_{84}Ni_{12}Co_4$ (red) in comparison to Pt/C (black) catalysts. The ORR tests were measured in O_2-purged 0.1 M $HClO_4$ solution at a sweep rate of 20 mV/s.

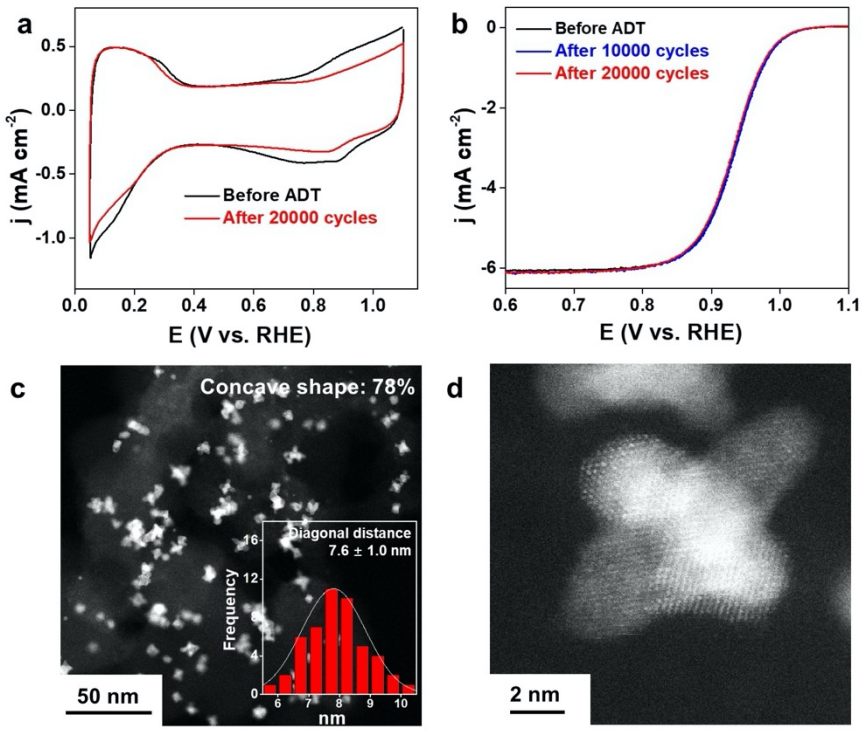

Supplementary Fig. 26 | Electrochemical stability analysis of sd-$Pt_{84}Ni_{12}Co_4$ catalysts. (**a**) CV comparison before (black) and after 20,000 cycles ADT (red). (**b**) ORR polarization curves of sd-$Pt_{84}Ni_{12}Co_4$ catalysts before ADT (black), after 10,000 cycles ADT (blue), and after 20,000 cycles ADT (red). (**c**, **d**) Representative HAADF-STEM and high-resolution HAADF-STEM image of the sd-$Pt_{87}Ni_{10}Co_3$-ADT after 20,000 cycles ADT. The insets of panel (**c**) are the percentage of concave shape and the size distribution, respectively.

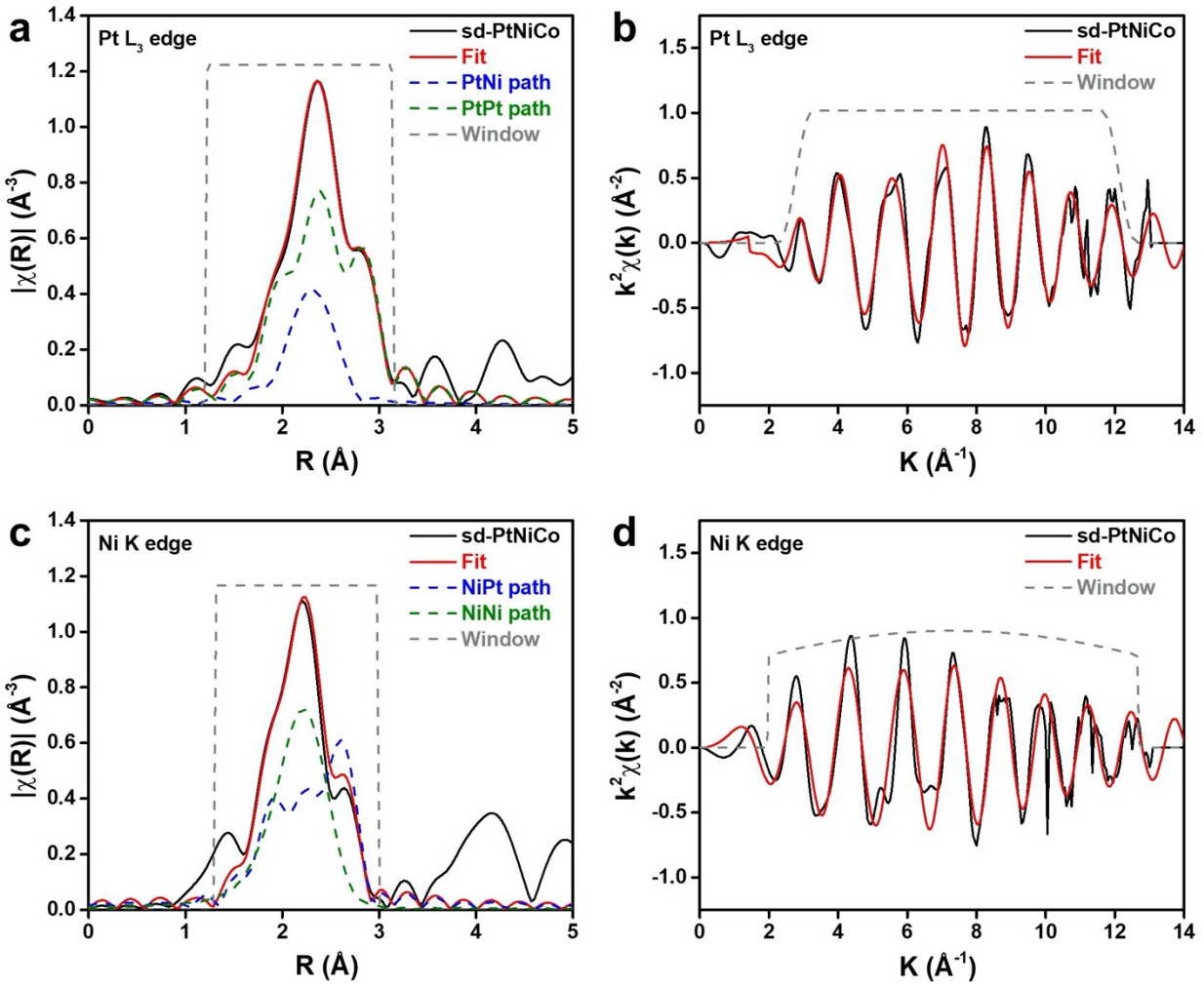

Supplementary Fig. 27 | In situ FT-EXAFS spectra at the Pt L_3-edge at the (a) R-space and (b) K-space and Ni K-edge at the (c) R-space and (d) K-space of sd-PtNiCo collected at 0.54 V in O_2-purged 0.1 M $HClO_4$ and their fits. Fits were performed at the Pt L_3 and Ni K-edge simultaneously in *R*-space, $k^{1,2,3}$ weighting. $1.2 < R < 3.1$ Å and $\Delta k = 2.8 - 12.2$ Å^{-1} for Pt spectra and $1.3 < R < 3.0$ Å and $\Delta k = 2.5 - 12.2$ Å^{-1} for Ni spectra were used for fitting. S_0^2 was fixed at 0.84 and 0.68 for Pt and Ni, respectively, as obtained by fitting the corresponding reference foils.

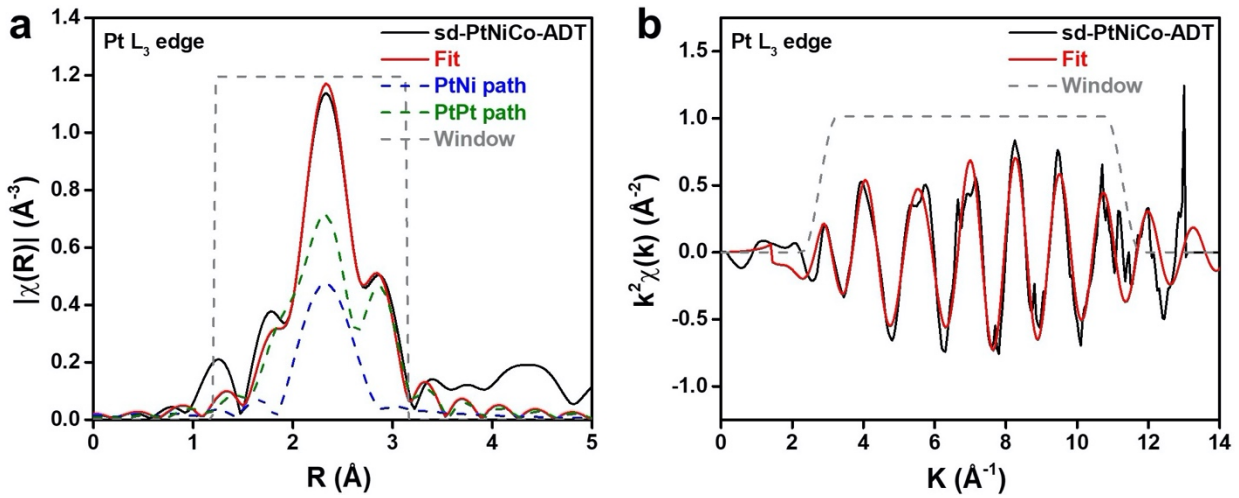

Supplementary Fig. 28 | In situ FT-EXAFS spectra at the Pt L_3-edge at the (a) R-space and (b) K-space of sd-PtNiCo-ADT collected at 0.54 V in O_2-purged 0.1 M $HClO_4$ and their fits. Fits were performed at the Pt L_3 in *R*-space, $k^{1,2,3}$ weighting. $1.22 < R < 3.14$ Å and $\Delta k = 2.77 - 11.29$ Å^{-1} were used for fitting. S_0^2 was fixed at 0.84 for Pt, as obtained by fitting the corresponding reference foil.

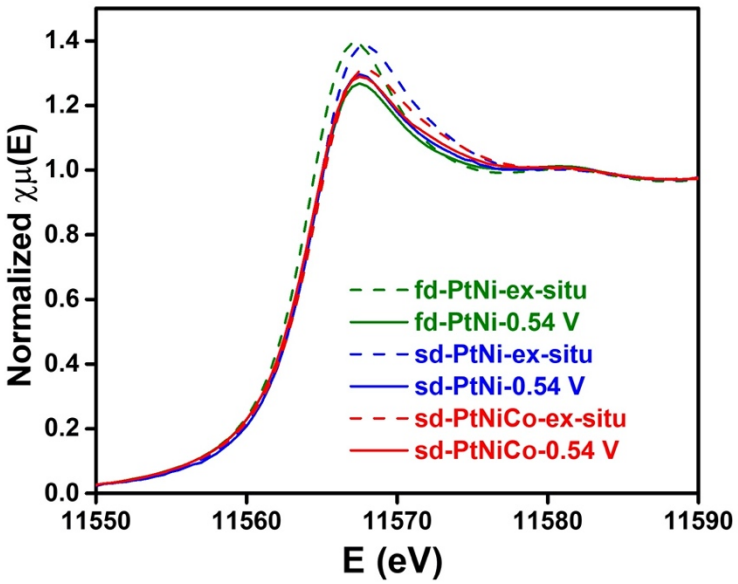

Supplementary Fig. 29 | Comparison of ex situ and in situ Pt L_3-edge XANES spectra of sd-$Pt_{85}Ni_{15}$, fd-$Pt_{86}Ni_{14}$, and sd-$Pt_{84}Ni_{12}Co_4$ catalysts. For each sample, the ex-situ spectrum was collected prior to in situ measurements. The in-situ spectrum was conducted at 0.54 V in O_2-saturated 0.1 M $HClO_4$ solution.

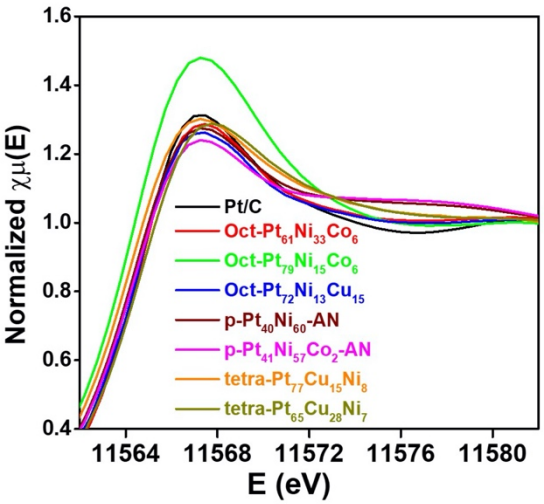

Supplementary Fig. 30 | *Ex-situ* experimental XANES spectra at the Pt L_3-edge of examined catalysts. All samples were electrochemically activated in N_2-purged 0.1 M $HClO_4$ solution at a sweep rate of 100 mV/s from 0.05 to 1.1 V vs. RHE prior to XAS measurement.

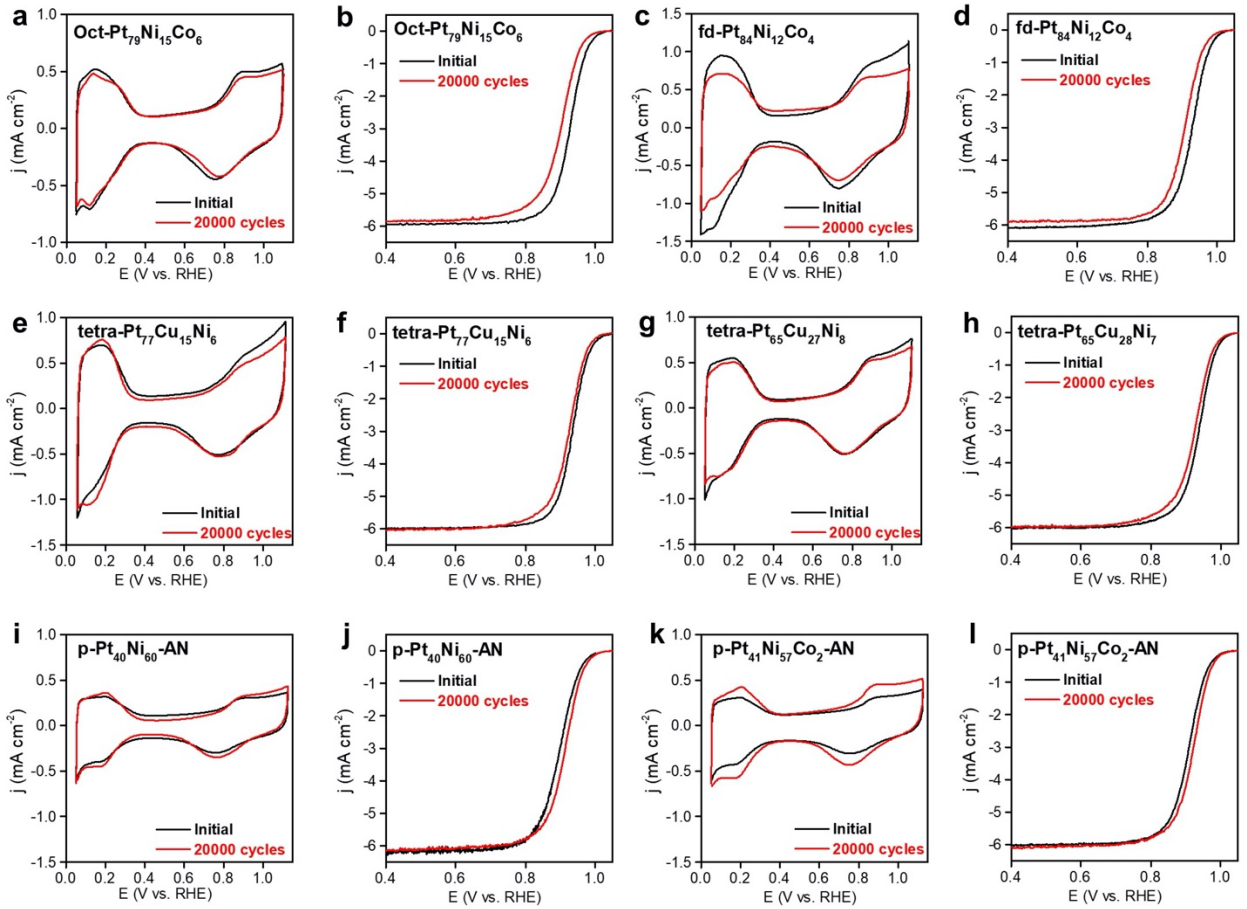

Supplementary Fig. 31 | Representative CVs and ORR polarization curves before (black) and after 20,000 cycles of ADT (red) for (a, b) Oct-$Pt_{79}Ni_{15}Co_6$ catalyst (Pt loading: 7 μg/cm^2). **(c, d)** fd-$Pt_{84}Ni_{12}Co_4$ catalyst (Pt loading: 7.5 μg/cm^2), **(e, f)** tetra-$Pt_{77}Cu_{15}Ni_8$ catalyst (Pt loading: 7.5 μg/cm^2). **(g, h)** tetra-$Pt_{65}Cu_{27}Ni_8$ catalyst (Pt loading: 7.5 μg/cm^2), **(i, j)** p-$Pt_{40}Ni_{60}$-AN catalyst (Pt loading: 7.5 μg/cm^2), **(k, l)** p-$Pt_{41}Ni_{57}Co_2$-AN catalyst (Pt loading: 7.5 μg/cm^2). The ADT was performed between 0.6 to 1.0 V versus RHE at a sweep rate of 100 mV/s in 0.1 M O_2-saturated $HClO_4$.

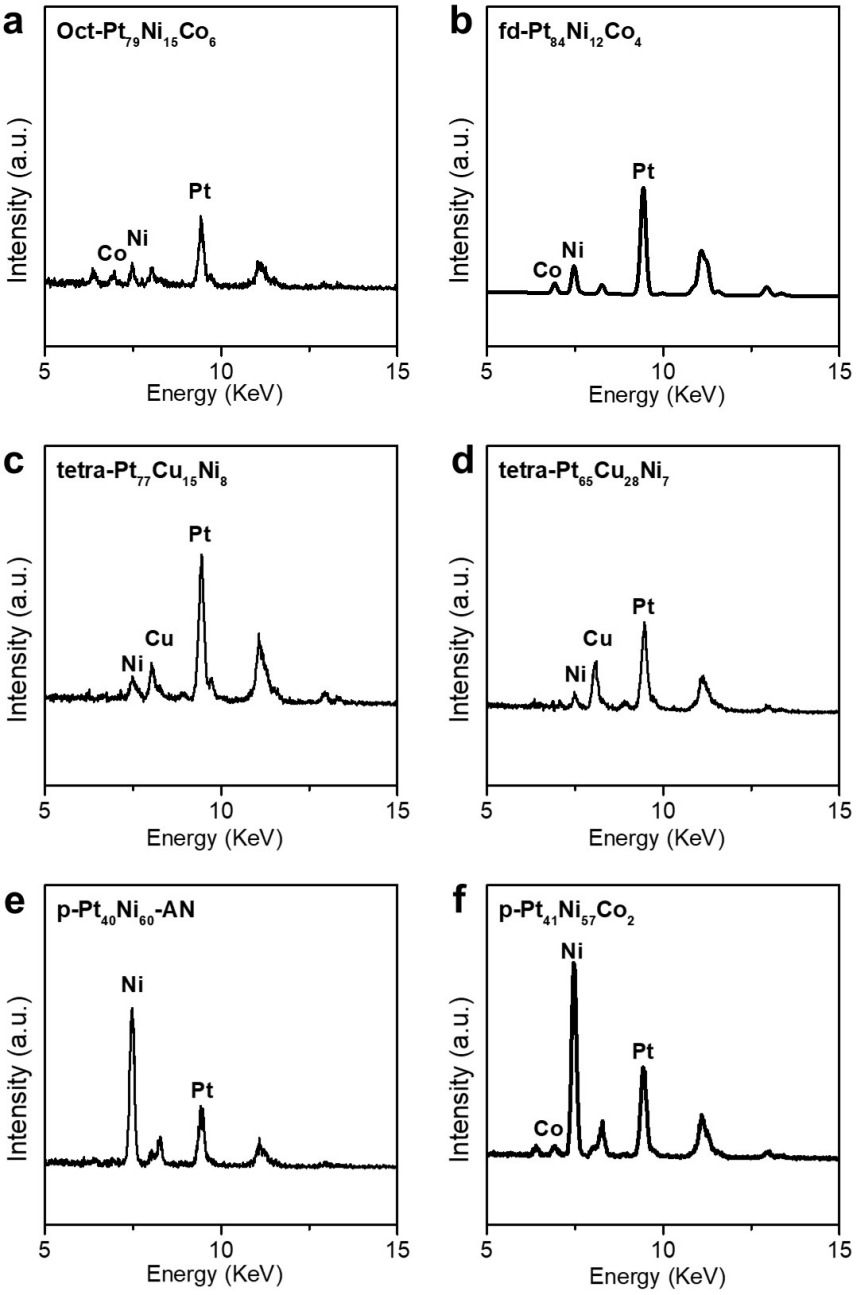

Supplementary Fig. 32 | Representative EDX elemental analysis for (**a**) Oct-$Pt_{79}Ni_{15}Co_6$ catalyst. (**b**) fd-$Pt_{84}Ni_{12}Co_4$ catalyst. (**c**) tetra-$Pt_{77}Cu_{15}Ni_8$ catalyst. (**d**) tetra-$Pt_{65}Cu_{28}Ni_7$ catalyst. (**e**) p-$Pt_{40}Ni_{60}$-AN catalyst. (**f**) p-$Pt_{41}Ni_{57}Co_2$-AN catalyst. All samples were electrochemically activated prior to EDX measurement.

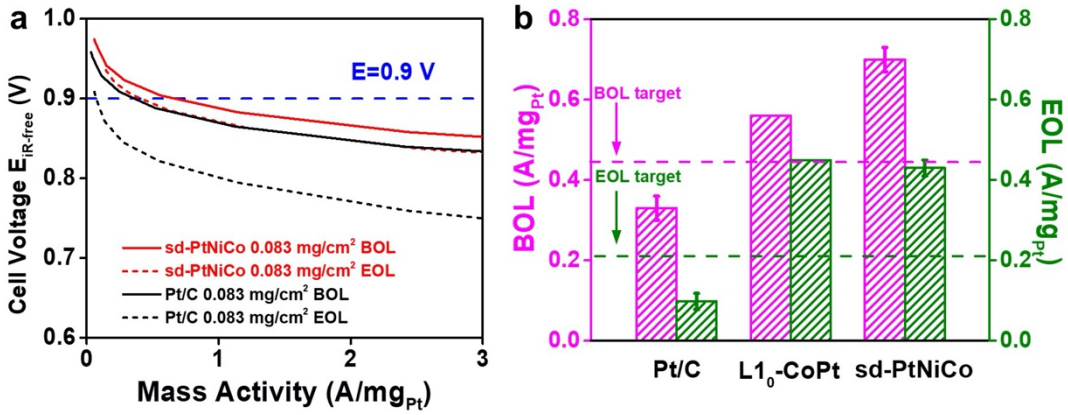

Supplementary Fig. 33 | MEA performance of the sd-PtNiCo catalysts. (**a**) MAs of sd-PtNiCo (red lines) and Pt/C (black lines) tested by measuring the current at 0.9 V (iR-free) under 150 kPa_{abs} H_2/O_2 (80 ºC, 100% RH) with correction for H_2 crossover. (**b**) Comparison of MAs of sd-PtNiCo, Pt/C, and $L1_0$-CoPt[2]. BOL: beginning of life. EOL: end of life. Cathode Pt loading is 0.083 mg_{Pt}/cm^2 for both Pt/C and sd-PtNiCo, and 0.105 mg_{Pt}/cm^2 for $L1_0$-CoPt, respectively. The error bars in MEA were determined from the standard deviation of 5 individual measurements.

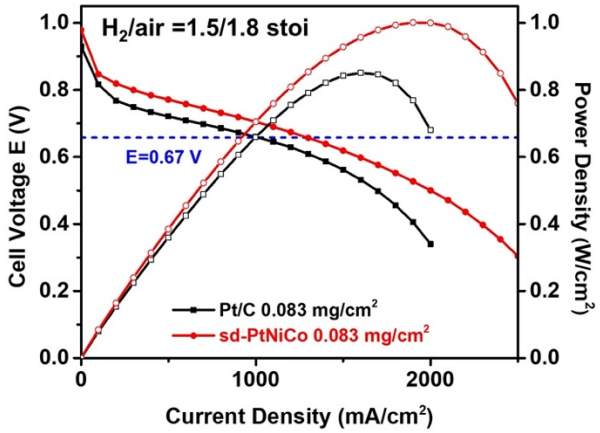

Supplementary Fig. 34 | MEA H_2-Air test comparison of sd-PtNiCo and Pt/C at 94 °C, 250 kPa_{abs} with a stoi of H_2/Air = 1.5/1.8.

Supplementary Tables

Supplementary Table 1 | Summaries of EXAFS fitting results of sd-Pt-alloys at the Pt L_3-edge. *: a fixed value.

Pt side			Pt-Pt scattering			Pt-M (M = Ni and/or Co) scattering			
	Stages	Composition	R_{Pt-Pt} (Å)	N_{Pt-Pt}	σ^2 (Å^2)×10^{-3}	R_{Pt-M}(Å)	N_{Pt-M}	σ^2 (Å^2)×10^{-3}	R factor
sd-$Pt_{85}Ni_{15}$	BOL	$Pt_{85}Ni_{15}$	2.71 ± 0.01	8.6 ± 1.4	9 ± 1	2.65 ± 0.01	1.5 ± 0.5	5 ± 2	0.005
	ADT	$Pt_{92}Ni_{8}$	2.73 ± 0.01	10 ± 2	9 ± 2	2.62 ± 0.06	0.7 ± 0.4	6 ± 3	0.002
sd-$Pt_{84}Ni_{12}Co_4$	BOL	$Pt_{84}Ni_{12}Co_4$	2.714 ± 0.007	8 ± 1	7.4 ± 0.9	2.65 ± 0.01	2.1 ± 0.6	9 ± 2	0.01
	ADT	$Pt_{87}Ni_{10}Co_3$	2.72 ± 0.03	9.6 ± 2.4	9 ± 3	2.67 ± 0.02	1 ± 1	2 ± 6	0.005
fd-$Pt_{86}Ni_{14}$	BOL	$Pt_{86}Ni_{14}$	2.733 ± 0.004	8.2 ± 0.7	6.6 ± 0.6	2.659 ± 0.007	1.2 ± 0.3	5 ± 1	0.007
	ADT	$Pt_{95}Ni_5$	2.746 ± 0.009	7.5 ± 1.4	5 ± 2	2.60 ± 0.02	1 ± 3	2*	0.013

*Fits were performed at the Pt L_3 and Ni K-edge simultaneously in *R*-space, $k^{1,2,3}$ weighting. Detailed fitting parameters and models used for fitting are given in the caption of the EXAFS fitting figure of each sample. BOL: beginning of life.

Supplementary Table 2 | Summaries of EXAFS fitting results of the Pt L_3-edge spectra of examined samples.

	Pt-Pt scattering			Pt-M (M = Ni and/or Co) scattering		
Sample	R_{Pt-Pt} (Å)	N_{Pt-Pt}	$\sigma 2$ (Å^2)$\times 10^{-3}$	R_{Pt-M}(Å)	N_{Pt-M}	σ^2(Å^2)$\times 10^{-3}$
fd-$Pt_{84}Ni_{12}Co_4$	2.717 ± 0.005	7.6 ± 1.3	5.6 ± 0.9	2.65 ± 0.02	2.7 ± 1.4	1.2 ± 0.4
fd-$Pt_{93}Ni_5Co_2$	2.727 ± 0.002	8.4 ± 0.5	6.1 ± 0.4	2.65 ± 0.01	1.7 ± 0.4	8 ± 2
p-$Pt_{40}Ni_{60}$-AN	2.68 ± 0.01	2 ± 1	5 ± 3	2.569 ± 0.004	7 ± 1	5 ± 7
p-$Pt_{41}Ni_{57}Co_2$-AN	2.68 ± 0.01	1.8 ± 0.7	3 ± 1	2.565 ± 0.002	7.3 ± 0.6	5.1 ± 0.5
tetra-$Pt_{65}Cu_{28}Ni_7$	2.696 ± 0.006	4.4 ± 1.0	5 ± 1	2.623 ± 0.008	3.8 ± 0.8	7 ± 2
tetra-$Pt_{77}Cu_{15}N_8$	2.700 ± 0.007	5.6 ± 1.0	5.8 ± 0.8	2.637 ± 0.009	3.3 ± 0.8	7 ± 2
Oct-$Pt_{72}Ni_{13}Cu_{15}$	2.713 ± 0.004	7.6 ± 7	NA	2.66 ± 0.01	1.9 ± 0.5	NA
Oct-$Pt_{79}Ni_{15}Co_6$	2.715 ± 0.009	6 ± 2	NA	2.63 ± 0.03	4 ± 2	NA
Oct-$Pt_{61}Ni_{33}Co_6$	2.722 ± 0.009	6.3 ± 1.9	6 ± 1	2.64 ± 0.02	1.4 ± 1.2	7 ± 6

Supplementary Table 3 | Summary of compressive strain, ΔAF, and activity.

Sample	Compressive strain (%)	ΔAF	Descriptor	Ln($SA_{PtM}/SA_{Pt/C}$)
sd-$Pt_{85}Ni_{15}$	1.45	0.43 ± 0.07	0.23	2.82
sd-$Pt_{92}Ni_{8}$-ADT	0.73	0.45 ± 0.02	0.14	2.74
sd-$Pt_{84}Ni_{12}Co_{4}$	1.31	0.49 ± 0.05	0.22	3.37
sd-$Pt_{87}Ni_{10}Co_{3}$-ADT	1.09	0.37 ± 0.07	0.18	3.33
fd-$Pt_{86}Ni_{14}$	0.62	0.27 ± 0.03	0.11	2.46
fd-$Pt_{95}Ni_{5}$-ADT	0.36	0 ± 0.03	0.04	1.76
fd-$Pt_{84}Ni_{12}Co_{4}$	1.20	0 ± 0.06	0.15	2.42
fd-$Pt_{93}Ni_{5}Co_{2}$-ADT	0.84	0 ± 0.06	0.11	1.80
Oct-$Pt_{72}Ni_{13}Cu_{15}$	1.27	0 ± 0.01	0.17	2.82
Oct-$Pt_{61}Ni_{33}Co_{6}$	1.20	0.08 ± 0.01	0.14	2.78
Oct-$Pt_{79}Ni_{15}Co_{6}$	1.09	0 ± 0.03	0.17	2.54
J-PtNWs	1.45	0	0.19	3.49
p-$Pt_{40}Ni_{60}$ AN	2.54	0.50 ± 0.05	0.38	1.68
p-$Pt_{41}Ni_{57}Co_{2}$ AN	2.54	0.45 ± 0.06	0.37	1.72
tetra-$Pt_{65}Cu_{28}Ni_{7}$	1.82	0.36 ± 0.08	0.27	2.74
tetra-$Pt_{77}Cu_{15}N_{8}$	1.82	0.41 ± 0.02	0.28	2.93
$L1_0$-$Pt_{50}Ni_{40}Co_{10}$	1.82	0.67	0.30	2.47
Cluster Model	**Compressive strain (%)**	**ΔAF**	**Descriptor**	**R_{Pt-Pt} (Å)**
Pt_{147}	0	0	0	2.774
sd-$Pt_{122}Ni_{25}$	2.06	0.3	0.3	2.717
fd-$Pt_{122}Ni_{25}$	1.58	0	0.20	2.730
sd-$Pt_{122}Ni_{17}Co_{8}$	2.1	0.31	0.3	2.716
sd-$Pt_{131}Ni_{16}$-ADT	1.15	0.25	0.18	2.742
fd-$Pt_{134}Ni_{13}$-ADT	0.76	0	0.10	2.753

Supplementary Table 4 | Calculated O binding energy on (111) sites and vertex sites.

Cluster model	ΔE_O^{111} (eV)	$\Delta E_O^{(Vertex)}$ (eV)
Pt_{147}	-3.62	-3.87
fd-$Pt_{122}Ni_{25}$	-3.48	-3.72
fd-$Pt_{134}Ni_{13}$-AST	-3.54	3.79
sd-$Pt_{122}Ni_{25}$	-3.31	-3.66
sd-$Pt_{131}Ni_{16}$-AST	-3.47 [-3.46 x 2; -3.50 x 1]	3.73 [-3.75 x 2; -3.69 x 1]
sd-$Pt_{122}Ni_{17}Co_8$	-3.316 [-3.32 x 2; -3.31 x 1]	-3.64 [-3.64 x 2; -3.64 x 1]
$L1_0$-$Pt_{116}Ni_{31}$	-3.37 [-3.38 x 2; -3.36 x 1]	-3.58 [-3.59 x 2; -3.57 x 1]

Supplementary Table 5 | Raw values of the energy of the calculated systems.

System	E(M) (Rydberg)	$E(M)–O_O^{111}$ (Rydberg)	$E(M)–O_O^{(Vertex)}$ (Rydberg)
O	-31.5474657724		
Pt_{147}	-12726.6522899304	-12758.4657118812	-12758.4841899013
fd-$Pt_{122}Ni_{25}$	-12709.2775256586	-12741.0807069197	-12741.0985388631
fd-$Pt_{134}Ni_{13}$-AST	-12717.4686235119	-12749.2763139104	-12749.2946718591
sd-$Pt_{122}Ni_{25}$	-12709.3537344255	-12741.1703392610	-12741.1443475557
sd-$Pt_{131}Ni_{16}$-AST	-12715.6410466914	-12747.4424207072 / -12747.4458790896	-12747.4637476077 / -12747.4594632346
sd-$Pt_{122}Ni_{17}Co_8$	-12617.6171547700	-12649.4087536697 / -12649.4078834565	-12649.4324942300 / -12649.4325123459
$L1_0$-$Pt_{116}Ni_{31}$	-12705.3514657628	-12737.1473333587 / -12737.1460702829	-12737.1628160048 / -12737.1613163246

Supplementary Table 6 | Summary of representative state-of-the-art ORR catalysts. *: Extracted from the literature; NA: not available.

Catalyst	SA (mA/cm²)		ADT Cycles	SA Retention	ECSA (m²/g)	MA (A/mg)
	BOL	ADT				
sd-$Pt_{84}Ni_{12}Co_4$ (this work)	**10.7**	**10.1**	**20,000**	**95%**	**68**	**7.1**
sd-$Pt_{85}Ni_{15}$ (this work)	**6.2**	**5.6**	**20,000**	**91%**	**65**	**4.0**
fd-$Pt_{86}Ni_{14}$ (this work)	**4.0**	**2.1**	**20,000**	**53%**	**65**	**2.6**
PtNi-BNCs/C[3]	5.16	5.17	50,000	100.2%	68.2	3.52
PtPb nanoplate/C[4]	7.8	7	50,000	89%	55	4.3
Pt_3Ni/C nanoframes[5]	8.4	NA	10,000	NA	67.2	5.7
PtNiCu[6]	6.2	3.86	30,000	62.4%	59	3.7
$Pt_{61}Ni_{33}Co_6$[7]	6.01	2.52	6,000	42%	46.5	2.8
Pt nanocage[8]	1.98	1.64	10,000	83.1%	38.2	0.75
$L1_0$-CoPt/Pt[2]	8.26	6.77	30,000	82%	27.3	2.26
C-$L1_0$-$PtNi_{0.8}Co_{0.2}$[9]	4.38	NA	10,000	NA	52	2.28
Mo-Pt_3Ni/C[10]	10.3	9.7	8,000	94%	67.7	6.98
J-PtNWs/C[11]	11.5	10.8	6,000	94.5%	118	13.6
PtNi c-Oct/C[12]	6.41	6.9	10,000	108%	34.6*	2.22

Supplementary References

1. Kitchin, J. R., Nørskov, J. K., Barteau, M. A. & Chen, J. G. Role of strain and ligand effects in the modification of the electronic and chemical properties of bimetallic surfaces. *Phys. Rev. Lett.* **93**, 156801 (2004).

2. Li, J. *et al.* Hard-magnet $L1_0$-CoPt nanoparticles advance fuel cell catalysis. *Joule* **3**, 124-135 (2019).

3. Tian, X. *et al.* Engineering bunched Pt-Ni alloy nanocages for efficient oxygen reduction in practical fuel cells. *Science* **366**, 850 (2019).

4. Bu, L. *et al.* Biaxially strained PtPb/Pt core/shell nanoplate boosts oxygen reduction catalysis. *Science* **354**, 1410 (2016).

5. Chen, C. *et al.* Highly crystalline multimetallic nanoframes with three-dimensional electrocatalytic surfaces. *Science* **343**, 1339-1343 (2014).

6. Cao, L. *et al.* Differential surface elemental distribution leads to significantly enhanced stability of PtNi-based ORR catalysts. *Matter* **1**, 1567-1580 (2019).

7. Zhao, Z. *et al.* Composition tunable ternary Pt-Ni-Co octahedra for optimized oxygen reduction activity. *ChemComm* **52**, 11215-11218 (2016).

8. Zhang, L. *et al.* Platinum-based nanocages with subnanometer-thick walls and well-defined, controllable facets. *Science* **349**, 412-416 (2015).

9. Wang, T. *et al.* Sub-6 nm fully ordered $L1_0$-Pt–Ni–Co nanoparticles enhance oxygen reduction via Co doping induced ferromagnetism enhancement and optimized surface strain. *Adv. Energy Mater.* **9**, 1803771 (2019).

10. Huang, X. *et al.* High-performance transition metal–doped Pt_3Ni octahedra for oxygen reduction reaction. *Science* **348**, 1230 (2015).

11. Li, M. *et al.* Ultrafine jagged platinum nanowires enable ultrahigh mass activity for the oxygen reduction reaction. *Science* **354**, 1414 (2016).

12. Zhu, E. *et al. In situ* development of highly concave and composition-confined PtNi octahedra with high oxygen reduction reaction activity and durability. *Nano Res.* **9**, 149-157 (2016).